Atmos. Chem. Phys. Discuss., 10, 22131–22218, 2010
www.atmos-chem-phys-discuss.net/10/22131/2010/
doi:10.5194/acpd-10-22131-2010

Atmospheric Chemistry and Physics Discussions

Airborne observations of the Eyjafjalla volcano ash cloud over Europe during air space closure in April and May 2010

U. Schumann[1], B. Weinzierl[1], O. Reitebuch[1], H. Schlager[1], A. Minikin[1], C. Forster[1], R. Baumann[1], T. Sailer[1], K. Graf[1], H. Mannstein[1], C. Voigt[1], S. Rahm[1], R. Simmet[1], M. Scheibe[1], M. Lichtenstern[1], P. Stock[1], H. Rüba[1], D. Schäuble[1], A. Tafferner[1], M. Rautenhaus[1], T. Gerz[1], H. Ziereis[1], M. Krautstrunk[2], C. Mallaun[2], J.-F. Gayet[3], K. Lieke[4], K. Kandler[4], M. Ebert[4], S. Weinbruch[4], A. Stohl[5], J. Gasteiger[6], H. Olafsson[7], and K. Sturm[8]

[1]Deutsches Zentrum für Luft- und Raumfahrt (DLR), Institut für Physik der Atmosphäre, Oberpfaffenhofen, Germany
[2]DLR, Flugexperimente, Oberpfaffenhofen, Germany
[3]Laboratoire de Météorologie Physique UMR 6016/CNRS, Université Blaise Pascal, Clermont-Fd, France
[4]Institut für Angewandte Geowissenschaften, Technische Universität Darmstadt, Germany
[5]Norwegian Institute for Air Research (NILU), Kjeller, Norway
[6]Meteorologisches Institut, Ludwig-Maximilians-Universität, München, Germany

[7] University of Iceland and Icelandic Meteorological Office, Reykjavik, Iceland, and University of Bergen, Norway
[8] Deutscher Wetterdienst, Offenbach, Germany

Received: 25 August 2010 – Accepted: 14 September 2010 – Published: 27 September 2010

Correspondence to: U. Schumann (ulrich.schumann@dlr.de)

Published by Copernicus Publications on behalf of the European Geosciences Union.

ACPD
10, 22131–22218, 2010

Abstract

Airborne measurements of Lidar backscatter, aerosol concentrations (particle diameters of 4 nm to 50 µm), trace gas mixing ratios (SO_2, CO, O_3, H_2O), single particle properties, and meteorological parameters have been performed in volcanic ash plumes with the Falcon aircraft operated by Deutsches Zentrum für Luft- und Raumfahrt (DLR). A series of 17 flights was performed over Europe between Southern Germany and Iceland during the eruption period of the Eyjafjalla[1] volcano between 19 April and 18 May 2010. Flight planning and measurement analyses were supported by a refined Meteosat ash product and trajectory model analysis. The volcanic ash plume was observed with Lidar directly over the volcano and up to a distance of 2700 km downwind. Lidar and in-situ measurements covered plume ages of 7 h to 120 h. Aged ash layers were between a few 100 m to 3 km deep, occurred between 1 and 7 km altitude, and were typically 100 to 300 km wide. Particles collected by impactors had diameters up to 20 µm diameter, with size and age dependent composition. Ash mass concentration was evaluated for a material density of 2.6 g cm^{-3} and for either weakly or moderately absorbing coarse mode particles (refractive index 1.59+0i or 1.59+0.004i). In the absorbing case, the ash concentration is about a factor of four larger than in the non-absorbing limit. Because of sedimentation constraints, the smaller results are the more realistic ones for aged plumes. The Falcon flew in ash clouds up to about 1 mg m^{-3} for a few minutes and in an ash cloud with more than 0.2 mg m^{-3} mean-concentration for about one hour without engine damages. In fresh plumes, the SO_2 concentration was correlated with the ash mass concentration. Typically, 0.5 mg m^{-3} ash concentration was related to about 100 nmol mol^{-1} SO_2 mixing ratio and 70 nmol mol^{-1} CO mixing ratio increases for this volcano period. In aged plumes, layers with enhanced coarse mode particle concentration but without SO_2 enhancements occurred. To first order, ash concentration and SO_2 mixing ratio in the plumes decreased by a factor of two

[1] Also known as *Eyjafjallajökull* or *Eyjafjöll volcano*, http://www.britannica.com/EBchecked/topic/1683937/Eyjafjallajokull-volcano

ACPD
10, 22131–22218, 2010

within less than a day. The ash plumes were often visible as faint dark layers even for concentrations below 0.1 mg m^{-3}. The ozone concentrations and the humidity inside the plumes were often reduced compared to ambient values. The large abundance of volatile Aitken mode particles suggests nucleation of sulfuric acid droplets. Ammonium sulfate particles were also found on the impactors. The effective diameters decreased from about 5 µm in the fresh plume to about 1 µm for plume ages of up to 6 days. The distal ash mass flux on 2 May was of the order 1800 kg s^{-1}; the SO_2 mass flux was about a factor of 3–4 smaller. The volcano ejected about 40 Tg of ash mass and 10 Tg of SO_2 during the whole eruption period. The results of the Falcon flights were used to support the responsible agencies in their decisions concerning air traffic in the presence of volcanic ash. The data described may be used for further studies, including comparisons to satellite and ground or space based Lidar observations, and for model improvements.

1 Introduction

Iceland's Eyjafjallajökull (63.63° N, 19.62° W, 1666 m a.s.l.) erupted on 14 April 2010 ejecting a volcanic ash (VA) plume over 9 km a.s.l. into the atmosphere (IES: Institute of Earth Sciences, University of Iceland, http://www.earthice.hi.is). Though the eruption of the Eyjafjalla volcano rates among the mid-sized eruptions (Mason et al., 2004; Mastin et al., 2009), it had strong impact on aviation over Europe. The eruption occurred in a weather situation with strong winds causing VA to drift within 1–2 days from Iceland toward Central Europe where it resided for several days, as observed, e.g., with ground based Lidar (Ansmann et al., 2010; Flentje et al., 2010). Advisories of areas at risk from the volcano plume were issued by the responsible Volcanic Ash Advisory Center (VAAC) of UK Meteorological Office based on model predictions. Based on these advisories, European aviation authorities decided on air space closure. As a consequence, air traffic ceased in 23 European countries and 75% of the European aerodrome network was closed, with more than 100 000 flights cancelled, affecting 10

ACPD
10, 22131–22218, 2010

million passenger journeys, in the time period 14 April to 20 April (as reported by EUROCONTROL). Further incursions of VA over Western Europe caused again airspace closures at various places and periods until 18 May 2010, leading to cancelling of about 7000 more flights.

Never before was such a large and busy air space impacted by a volcanic eruption. So far, air space was closed whenever any notable trace of VA was expected in the air space without specifying an acceptable safety limit of ash loading (Casadevall, 1993). In desert vicinity regions, such as Saudia Arabia, annual mean dust mass levels of $0.2\,mg\,m^{-3}$ are not uncommon (Schütz, 1980; Weinzierl et al., 2009). In comparison to desert dust, VA is considered more dangerous because of its lower melting temperature (Casadevall, 1993). During the past 30 years, more than 120 airplanes have inadvertently flown through clouds of VA from erupting volcanoes (Webley and Mastin, 2009). In a few cases, serious engine or aircraft damages have been reported, after a few minutes of flight time in volcanic plume with ash loading of possibly $2\,g\,m^{-3}$ as estimated from engine damage analysis (Dunn and Wade, 1994; Przedpelski and Casadevall, 1994). Shortly after the Eyjafjalla eruption, since 20 April 2010, aviation experts agreed preliminarily on new thresholds: $0.2\,mg\,m^{-3}$ as the limit below which aircraft may fly without special attention, and $2\,mg\,m^{-3}$ as the limit above which flights should be avoided. At the end of this volcanic eruption (since 19 May), areas with low ($<0.2\,mg\,m^{-3}$), medium (0.2 to $2\,mg\,m^{-3}$) and high ($>4\,mg\,m^{-3}$) contamination were distinguished (ICAO, 2010) by the UK Meteorological Office.

A few airborne studies have been performed in distal plumes of eruptive volcanoes before, as reviewed in Watson and Oppenheimer (2001). The concentrations and fluxes of trace gases were measured in the Mt. St. Helens plume in 1980 (Bandy et al., 1982; Cronn and Nutmagul, 1982). The SO_2 concentration reached $440\,nmol\,mol^{-1}$, CO was in the order of $200\,nmol\,mol^{-1}$. Source rates of SO_2 of up to 10 and $140\,kg\,s^{-1}$ were derived for Mt. St. Helens and Mt. Redoubt, respectively (Hobbs et al., 1982, 1991). Aircraft and balloon-borne measurements were made of trace gases, atmospheric particles, and condensed acid volatiles in the plume of El Chichón volcano,

ACPD
10, 22131–22218, 2010

Mexico, in November 1982 (Kotra et al., 1983; Arnold et al., 1990). Hydrogen sulfide was the primary gaseous sulfur species in that plume. Lidar and in-situ measurements were used to determine the cross-sectional area and the fluxes of particles and gases from the Mt. Redoubt Volcano in 1990 (Hobbs et al., 1991). The young stratospheric plume of the Mt. Pinatubo eruption in June 1991 was observed mainly by remote sensing techniques, including airborne Lidar (Winker and Osborn, 1992; McCormick et al., 1995). The volcanic eruptions of the Mt. Okmok (53.4° N, 168.1° W; 12 July 2008) and Mt. Kasatochi (52.2° N, 175.5° W; 7 August 2008) injected about 1.7 Mt SO_2 into the atmosphere. The eruption reached up to the stratosphere in 15.2 km altitude and resulted in a cancellation or delay of 44 aircraft flights. Increased SO_2 (and particulate sulfate) concentrations up to 0.5 nmol mol^{-1} was repeatedly detected in the lower stratosphere above Europe up to 4 months after eruption (Martinsson et al., 2009; Heue et al., 2010; Jurkat et al., 2010; Schmale et al., 2010; Voigt et al., 2010). In February 2000, a 33–34 h aged volcanic cloud from Hekla volcano, Iceland, was incidentally encountered by the DC-8 research aircraft during a larger atmospheric observation experiment (Hunton et al., 2005; Rose et al., 2006). During this flight, the DC-8 sampled various gaseous (including SO_2, HCl and HF) and particulate properties at 10.4 km altitude, for about 12 min inside a cirrus cloud. The SO_2 concentration exceeded 1 µmol mol^{-1}. Engine damages diagnosed for this case (perhaps for other reasons) were later interpreted indicating that flying in even minor VA plume remnants may cause major damage to the aircraft (Grindle and Burcham Jr., 2002, 2003; Pieri et al., 2002).

The size spectra of ash particles available in the literature were mostly derived from tephra deposited at ground (Rose and Durant, 2009; Webley and Mastin, 2009). Samples taken at ground near the Eyjafjallajökull indicate particle sizes up to 300 µm, with more than 50% mass in particles larger than about 50–150 µm, varying during the eruption period (T. Thorsteinsson, personal communication, 2010 http://www.earthice.hi.is/page/ies_EYJO2010_Grain). Most of the large particles sediment out of the ash plume in close vicinity of the volcano.

ACPD
10, 22131–22218, 2010

Only a few airborne measurements of the ash size spectrum and total mass concentrations have been taken inside VA plumes (Hobbs et al., 1982). Particle counters inside the fuselage measure only small particles (<2 µm) because of strong losses at the inlets (Hunton et al., 2005). Larger particles can be measured by particle counters mounted outside the fuselage, but care is needed to separate ash particles from cloud particles. For example, the particle size distribution measured in the Hekla ash plume is dominated by cirrus ice crystals (Rose et al., 2006). The mass concentration of ash particles, which is essential for this study, cannot be directly measured. The volume concentration can be derived from particle number size distributions derived from optical laser aerosol spectrometer measurements (Weinzierl et al., 2009). Such spectrometers count the particles and measure the amount of light scattered by single particles into the collection optics of the particular instruments. The particle size must be analyzed from the measured amount of light, which requires knowledge of the light scattering for the given geometry. The scattering is a function of complex refractive index and shape of the particles (Mishchenko and Travis, 1994; Borrmann et al., 2000). The optical properties of VA particles (and their material density) are not well known but can be estimated once the composition of the particles is known (Patterson et al., 1983; Kandler et al., 2009).

The predictions of ash plumes by the UK VAAC are based on a Lagrangian model (Jones et al., 2007), which computes the trajectories of ash particles as a function of ambient winds. The results of this and similar models depend crucially on the volcanological input data, such as plume height, mass eruption rate, eruption duration, ash distribution with altitude, and particle-size distribution. These inputs must be assigned in real time during an event, often with limited observations (Webley and Mastin, 2009). Moreover, the results depend strongly on the meteorological fields used for computing the plume transport, and on particle sedimentation and deposition, and possibly on changes of particle properties during the long-range plume transit. Therefore, observations are important for assessing and improving the quality of the volcanic plume predictions.

ACPD
10, 22131–22218, 2010

Besides the obvious operational implications, the impact of VA and gaseous emissions on the atmosphere is of high scientific interest. Volcanic emissions may contribute to changes of air composition and cloudiness. Much can be learned about atmospheric chemistry and cirrus formation (Hunton et al., 2005; Rose et al., 2006; Durant et al., 2008) from well-instrumented flights in VA layers. We were in particular interested in understanding the plume dispersion, the ash particle properties, and the chemical plume composition. The data are of interest also for validation of Lidar and satellite based aerosol and sulfur dioxide (SO_2) observations.

Between 19 April and 18 May 2010, we performed measurements in VA plumes with the research aircraft Falcon of the Deutsches Zentrum für Luft- und Raumfahrt (DLR). The measurements were supported by satellite data analysis, VA model predictions, and weather forecasts. The principal motivation of these measurement flights was to provide as quickly as possible airborne measurements of VA plume properties over Central Europe. The data should provide information useful to assess the VA load predictions, which were used in the decisions on air space closure over Central Europe. This paper describes the Falcon measurements, summarizes the data obtained and presents some early analyses and experiences. It should serve as a basis for more detailed analyses and upcoming studies.

2 Experimental methods

2.1 Falcon measurement system

The Falcon 20E, a twin-engine jet aircraft, see Fig. 1, was built by Dassault in 1975. The turbofan jet engines of type Honeywell TFE 731-5BR-2C (2×21 kN thrust) were renewed in 1995. The aircraft ceiling is 12.8 km, cruise speed near 200 m s^{-1}, endurance about 4.5 h, with about 3100 km range. The aircraft has been used in recent years for many atmospheric research projects (Schlager et al., 1997; Schumann et al., 2002; Minikin et al., 2003; Gayet et al., 2006; Reitebuch et al., 2009; Weinzierl et al., 2009;

ACPD
10, 22131–22218, 2010

Voigt et al., 2010). In particular, the Falcon has been measuring in desert dust regions at dust loads of up to 5 mg m^{-3}, without notable damage to the engines (Weinzierl et al., 2009).

For the VA flights, the aircraft had been instrumented within a few days after the volcanic eruption onset with instruments that were available quickly from previous experiments, see Table 1. The instruments include a Lidar, in-situ instruments for aerosol microphysics, chemical species, and meteorological parameters like temperature, humidity and wind. Furthermore, aircraft parameters (position, aircraft speed etc.) were recorded. The 2D-C and the particle impactor instruments, see Table 1, were provided by the Laboratoire de Météorologie Physique, Clermont-Ferrand and by the Technical University Darmstadt, respectively. All other instruments were provided by DLR. For possible early detection of engine damages, the pilots controlled temperature and pressure indicators for normal engine operations during flight. Satellite (Iridium) telephone connections were available and important for real-time communication of the results from the observers on board to the decision-making agencies.

2.1.1 Lidar

The 2-µm Doppler wind Lidar (Light detection and ranging) was deployed on the Falcon aircraft in a downward looking direction performing conical scans for the retrieval of vertical profiles of the horizontal wind vector and attenuated aerosol backscatter. The coherent, heterodyne-detection Lidar is based on a transceiver unit from Lockheed Martin Coherent Technologies. The laser is transmitting pulses with a wavelength of 2.02 µm, length of 400 ns, energy of 1–2 mJ, and a repetition rate of 500 Hz (Köpp et al., 2004). Measurements are obtained from an altitude of 400 m below the aircraft to the ground with a vertical resolution of 100 m. The wind vector is derived by a velocity-azimuth-display technique from 20 line-of-sight (LOS) directions during one conical scan with a horizontal resolution of 4–6 km depending on aircraft ground speed (Reitebuch et al., 2001). Accuracies of better than 1 m s^{-1} can be achieved for the horizontal wind speed (Weissmann et al., 2005a,b). The backscatter signal is obtained after averaging a num-

ACPD
10, 22131–22218, 2010

ber of 500 laser pulse-returns during 1 s for each LOS and applying a correction for range R with a factor of R^2. Thus, the signal profiles are obtained with a horizontal resolution of 150–200 m for typical aircraft speeds. The range-corrected signal depends on the vertical profile of the atmospheric backscatter and extinction coefficient, which are both depending on the particle (aerosol, cloud, ash) content of the atmosphere, their size distributions and scattering properties. The 2-µm laser wavelength is higher than the typical wavelengths of up to 1.064 µm for ceilometers (Flentje et al., 2010) or aerosol Lidars (Ansmann et al., 2010), which were used to observe the VA plumes from the ground. Thus, the 2-µm Lidar observations complement those ground observations for a wavelength, which is comparable to the size of the VA particles. The heterodyne detection method is more sensitive to lower aerosol contents in the atmosphere compared to a direct-detection aerosol Lidar, because the heterodyne signal is analyzed in a much lower frequency bandwidth, making it insensitive to the solar background. On the other hand, the volume backscatter and extinction coefficient cannot be derived directly from the heterodyne signal, as it is performed for aerosol Lidars (Ansmann et al., 2010). Nevertheless, the real-time display of the signal-to-noise ratio was used during flights to detect the presence of VA layers, their vertical and horizontal extent and their relative signal strength compared to water or ice clouds. Thus, the Lidar observations were essential as a pathfinder for subsequent in-situ observations.

In the post-flight analysis, the lower and upper boundary of the measured VA layers was determined from the range-corrected attenuated backscatter signal of the Lidar by visual inspection. Layers were assigned where they were clearly separated vertically from the atmospheric aerosol boundary layer, showed signal levels lower than from water clouds but higher than typically observed in the free troposphere, and are characterized by a strong signal gradient. As the VA layers showed high signal levels combined with high signal gradients within 100–200 m, the upper and lower boundaries could be clearly identified. The uncertainty in the determination of the VA layer boundaries is ±150 m resulting from the range resolution of the Lidar (±50 m) and the applied threshold on the signal strength and gradient (±100 m).

ACPD
10, 22131–22218, 2010

2.1.2 In-situ aerosol instruments

The in-situ aerosol instrumentation covered the whole particle size spectrum including particles in the nucleation mode (4–10 nm), Aitken mode (10–160 nm), accumulation mode (160 nm–1 µm), coarse mode (1–50 µm) and particles in the far super-micron diameter range (up to 800 µm). The super-160 nm particle fraction was sized by a combination of optical particle counters: Optical Particle Counter (OPC), Passive Cavity Aerosol Spectrometer Probe (PCASP), and Forward Scattering Spectrometer Probe (FSSP) of type Grimm SKY-OPC 1.129, PMS PCASP-100X, and PMS FSSP-300 (Weinzierl et al., 2009), see Table 1. The measurement principle of these instruments is the sizing of particles based on the detection of the amount of light scattered by single particles. The instruments convert the scattering signal into an electrical signal, which corresponds to size information and is resolved into an array of channels which is fixed in case of the three aerosol spectrometers used in this study. The instruments differ mainly in optical geometry and electronic signal processing, and, as a result, cover different particle size ranges. According to the manufacturers, the PCASP covers nominally the size range 0.12–3.5 µm (15 channels), the OPC 0.25–32 µm (31 channels) and the FSSP 0.3–20 µm (31 channels). During the Falcon flights discussed in this study, we found the FSSP to show false counts due to electronic noise in some lower channels as well as in the two highest channels, and these channels were disregarded in the data analysis, therefore. For the PCASP the two lowest channels were disregarded, raising the lower end of the PCASP size range to approx. 0.16 µm. Below this size, the total number of particles larger than 4 nm and larger than 10 nm is known from CPC measurements which were operated at different cut-off diameters (Schröder and Ström, 1997). In addition to the total size distribution, the size distribution of the non-volatile aerosol compounds was also measured. For this purpose, a second optical particle counter of type Grimm SKY-OPC 1.129 and two of the CPCs were connected to a thermal denuder heating the aerosol to 250 °C. The heating temperature of the thermal denuder allows the separation of high to medium volatile organics and com-

ACPD
10, 22131–22218, 2010

ponents of sulfuric acid-like and ammonium sulfate-like behavior from non-volatile or refractory components like crustal material in VA layers (Clarke, 1991). The size range from about 25 to 800 µm, depending on airspeed, was covered by the 2D-C probe (Lawson et al., 2006; Gayet et al., 2009). The 2D-C instrument records the two-dimensional shadows of particles as they pass through a focused laser beam and provides information about particle shape and size from the analysis of the recorded shadow. Beyond particle sizing, the instrumentation was designed to provide information on the aerosol absorption coefficient at the wavelengths of 467, 530 and 660 nm with a 3-λ Particle Soot Absorption Photometer (PSAP) (Virkkula, 2010). These absorption data can be used to determine the complex refractive index of aerosols (Petzold et al., 2009). Three impactor-sampling devices were mounted inside the aircraft to collect VA particles for off-line single particle analysis (Ebert et al., 2002; Kandler et al., 2009). The PCASP, FSSP, 2D-C, and a Giant Particle Collector (GPaC) were mounted under the wings of the aircraft. All other instruments were operated in the cabin, sampling air from the Falcon aerosol inlet, which is sampling in forward direction close to isokinetic sampling conditions. For large particles, the sampling efficiency of this inlet falls off rigorously. The cut-off diameter, at which 50% of the particles pass the isokinetic inlet, depends on outside pressure and air speed. For typical Falcon speed, the cut-off is near 2.5 µm at ground level and decreases to about 1.5 µm at 10 km altitude (Fiebig, 2001; Wendisch et al., 2004).

2.1.3 Method for derivation of the ash mass concentration

The mass concentration of ash particles is derived from particle number size distributions measured by the three optical laser aerosol spectrometers, PCASP, OPC, FSSP, specified above (Table 1). The amount of light scattered by a single particle into the instrument's collection optics depends on particle size, the complex refractive index and the shape of the particle.

In the literature, many papers discuss the refractive index of mineral dust (Balkanski et al., 2007; Petzold et al., 2009), but only a few data for volcanic ash are reported.

ACPD
10, 22131–22218, 2010

For visible wavelengths, the real part of the refractive index varies between 1.5 and 1.6 for silicate glasses similar to volcanic ashes (Patterson, 1981) and between 1.48 and 1.57 for naturally occurring rocks (obsidian, basaltic glass and andesite) (Pollack et al., 1973). While the size distributions for small particles (OPC, PCASP) are rather insensitive to the variation of the imaginary part of the refractive index, this is not the case for the FSSP instrument (Weinzierl et al., 2009) because it is much more selective for forward scattering angles only. With increasing particle absorption, the size distribution of the FSSP in general shifts towards larger particle sizes. The imaginary part of the refractive index of volcanic ash varies widely. Values between 0.00027 and 0.0015 have been reported for naturally occurring rocks (Pollack et al., 1973). Patterson et al. (1983) investigated ash samples of the 1982 El Chichón eruption collected at three surface sites at distances between 12 and 80 km from the volcano. The imaginary part of the refractive index at 632 nm (the laser wavelength of the PCASP and FSSP) decreased from about 0.0015 for the sample collected at a distance of 12 km to the vent to 0.0008 for an 80 km distance sample. Clarke et al. (1983) obtained a value of 0.0034 at 550 nm for the imaginary part of the El Chichon ash. Patterson (1981) found an imaginary part of the refractive index for Fuego ash of 0.02 at 650 nm. In this study, the refractive index value is derived from the composition of particles collected by the impactors.

In the analysis of the particle size distributions of the optical aerosol spectrometer probes, we use Mie calculations assuming spherical particles. The channels are grouped into larger size bins to account for ambiguities in the Mie scattering cross section as a function of particle size, to improve counting statistics in particular for high channel numbers, and to smooth the resulting size spectra. To estimate the impact of particle non-sphericity of ash particles (Munoz et al., 2004) we assessed the instrument response of the FSSP-300 by T-matrix calculations for randomly-oriented prolate spheroids (Mishchenko and Travis, 1998). In principle, prolate ice particles cause a shift in size distribution towards lower sizes, decreasing total mass concentration (Borrmann et al., 2000).

ACPD
10, 22131–22218, 2010

The mass distribution follows from the volume distribution after multiplication with the particle density ρ_P. The density of ash particles including rock fragments varies from 0.7 to 3.2 g cm^{-3}. (http://volcanoes.usgs.gov/ash/properties.html#density). Here, the density ρ_P is estimated based on the impactor samples of 2 May 2010, see below. We assumed ρ_P=2.6 g cm^{-3} to hold for all VA layers investigated in this study.

2.1.4 Trace gas instruments

The trace gases ozone (O_3), carbon monoxide (CO), and sulfur dioxide (SO_2), and water vapor (H_2O) were measured with in-situ instruments inside the cabin. The individual instruments in the fuselage sampled air through rearward facing inlets mounted on top of the Falcon. Teflon (PFA) was used for the inlet tubes of the SO_2 and O_3 instruments to avoid wall losses. The inlet tubing of the CO instrument was stainless steal.

Sulfur dioxide was measured using pulsed fluorescence (Luke, 1997). The instrument deployed was a Thermo Electron SO_2 Analyzer (Model 43C Trace Level). In the optical cell of the instrument, SO_2 is electronically excited by radiation in the wavelength range 190–230 nm generated by a Xenon flash lamp pulsed at 10 Hz. Excited SO_2^* is partly quenched and photolyzed, and partly fluoresces at 320 nm. This radiation is detected by a photomultiplier tube. The photomultiplier sampling gate is delayed by 30 µs from the trigger of the flash lamp to reduce electronic noise associated with the flash. The fluorescence intensity is linearly proportional to the SO_2 mixing ratio. The fluorescence technique is subject to a weak positive interference from aromatic hydrocarbons, CS_2 and NO. Hydrocarbons are removed from the sample air in the instrument by diffusion through a semi-permeable membrane (hydrocarbon kicker). Rejection ratios (ratio of the concentration of interferant to SO_2 required to produce an equivalent instrument signal) for CS_2 and NO were determined in laboratory experiments to 20 (Luke, 1997) and 35 (Roiger, 2007), respectively. Interferences from CS_2 and NO are considered to be negligible for the present measurements in view of observed CS_2/SO_2 and NO/SO_2 concentration ratios of about 0.01 (Cronn and Nut-

ACPD
10, 22131–22218, 2010

magul, 1982) and 0.001 (Rose et al., 2006) in volcanic plumes. The detection limit of the SO_2 monitor is 0.2 nmol mol^{-1}. The precision and accuracy are 3% and 5%, respectively. The response time of the instrument is 80 s ($t_{95\%}$).

Ozone was measured with a Thermo Environment ultra-violet (UV) photometric ozone analyzer (Model 49C). The instrument employs a mercury lamp to produce UV light at a wavelength of 254 nm. The degree of absorption of the UV light is linearly proportional to the ozone concentration in the optical cell. The sample air drawn into the instrument is passed to two optical cells, one equipped with an ozone scrubber to serve as a reference gas. The flow to the reference and measurement cell is alternated every 4 s using solenoid valves. The light intensity of each cell is measured by separate detectors. A particle filter (Teflon, 5 micro pore) is installed upstream of the optical cells to avoid scattering or absorption of UV light by particles. A weak interference of the UV absorption technique with SO_2 (rejection ratio of 70) was considered during data reduction. The detection limit and response time of the instrument is 1 nmol mol^{-1} and 15 s with a 10 s lag time. Precision and accuracy are 3%/1 nmol mol^{-1} (whichever is larger) and 5%, respectively.

Carbon monoxide was measured using a fast-response (<2 s) vacuum UV resonance fluorescence detector (Model AEROLASER AL 5001). UV light at a wavelength of 150 nm is mirrored by an optical filter into a fluorescence cell. The light is produced by a resonance lamp excited by a radio frequency discharge. The fluorescence is detected by a photomultiplier tube. The detection limit of the instrument is 3 nmol mol^{-1}. Precision and accuracy are 3% and 5%, respectively (Gerbig et al., 1999).

Water vapor was measured with two independent instruments: a Lyman-α absorption water vapor instrument operated by the DLR flight department and a dew point hygrometer (Voigt et al., 2010). The Lyman-α instrument has an accuracy of 5% for humidity mass concentration above 10^{-4}. Humidity data with 10 Hz time resolution are available at altitudes below 8 to 9 km. The dew point hygrometer CR-2 (Buck Research Instruments) measures the temperature of a mirror carrying a thin dew or frost layer held in equilibrium with the ambient water vapor. The detection limit of the frost point

ACPD
10, 22131–22218, 2010

hygrometer is better than 1 µmol mol^{-1} for a time resolution of 2 s. The uncertainty in the water vapor mixing ratio is mainly determined by the uncertainty in the temperature measurement and amounts to ±8%. This uncertainty does not include oscillations of the mirror temperature induced by the control circuit after steep gradients in humidity, which have to be removed from the data set. Hence, depending on water vapor gradients the response time of the frost point hygrometer is in the order of one minute to few seconds. The ambient air temperature was measured with an accuracy of 0.3 K with a PT100 sensor with a Rosemount inlet.

2.2 Modeling methods

For flight planning (see below) and for analysis of the plume age and source altitude and the source strength at time of emission at the volcano, we use the FLEXPART model (at Norwegian Institute for Air Research (NILU) and DLR) and the HYSPLIT model (at DLR) in backward or forward mode driven with different meteorological reanalysis data. The use of different models, different atmospheric datasets and different methodologies serves to provide a first guess of the robustness of the corresponding results.

The FLEXPART model (Stohl et al., 2005) driven with ECMWF reanalyzed data with 0.5°×0.5° horizontal resolution is used for age analysis from backward trajectories of virtual particles released at the points of measurements along the flight paths. The backward transport method accounts for turbulence and convection and has been validated by comparison to other methods (Seibert and Frank, 2004). For each grid cell along the flight tracks, 10 000 particles are released. The particles are classified as passing over the volcano when approaching the volcano within 50 km distance. For those particles, the information of altitude, time, release point, release time and residence time over the volcano were kept. Some particles passed over the volcano several times so that their ages spread over several hours or even days. Besides minimum and maximum ages, we report the age occurring most frequently as best estimate.

ACPD
10, 22131–22218, 2010

Alternatively, the ash-plume age was computed using the National Oceanic and Atmospheric Administration (NOAA) Air Resources Laboratory (ARL) HYSPLIT model (Draxler and Hess, 1998; Draxler, 2003). The model was driven with reanalyzed atmospheric data from the Global Forecast System/Global Data Analysis System (GFS/GDAS) model. The calculations were performed using GFS data with $0.5^\circ \times 0.5^\circ$ or $1^\circ \times 1^\circ$ horizontal resolution. The physics in HYSPLIT was parameterized using the recommended standard settings. For the forward simulations, the Eyjafjalla ash emission was modeled using a vertical line source located at the volcano with varying mass flow rate and vertical extent. The top height h_t of the source was taken from the 6-hourly updated graphics issued by the VAAC (files on http://www.metoffice.gov.uk/aviation/vaac/vaacuk_vag.html). The bottom end of the line source was estimated to be $0.5 * (h_{t,min} - h_S)$, were h_S is the volcano height and $h_{t,min}$ the minimum top-height reported for the 6-h period. The mass flow rate is computed from

$$\dot{m} = \dot{m}_{ref} \left(\frac{h_t - h_S}{h_{t,ref} - h_S} \right)^{1/a} \quad (1)$$

using a=0.25, which is between the values 0.241 and 0.259 given in Mastin et al. (2009) and Sparks et al. (1997), respectively. The reference mass flow rate $\dot{m}_{ref}$ was adjusted such that the total ash mass ejected during the first 72 h of the volcano eruption equals the total airborne tephra mass, m_t times the fraction of fine-grained ash below 63 µm, m_{63} (grain size Φ=4). For m_t an average value of 5×10^5 kg s^{-1} during the first three days was used according to the preliminary estimates published by the IES (http://www.earthice.hi.is/page/ies_Eyjafjallajkull_eruption, estimates an average discharge rate of 7.5×10^5 kg s^{-1} with ±50% uncertainty, about two-thirds of which have gone airborne). A lower bound of the fine ash fraction m_{63} was estimated to be ≥3% from an ash sample taken 2 km west of the active vent on 28 April (Björn Oddsson, IES, http://www.earthice.hi.is/page/ies_EYJO2010_Grain). The true fine-ash mass fraction in the eruption column is probably larger if we consider that the largest particles fall out fastest and hence the ground samples may underestimate the finer

ACPD
10, 22131–22218, 2010

particle's frequency. The total "fine" ash mass was distributed equally on six representative ash particle size classes with diameters of 2, 6, 15, 25, 40 and 60 µm, which are handled in HYSPLIT as different pollutant species in order to account for the different sedimentation velocity of the particles. Figure 2 shows the time-series of the source characteristics as used in this study. For a given point of measurements, an ensemble of backward trajectories was computed, to obtain a first estimate of the plume age and source altitude at the time of eruption. The results were checked and corrected based on forward trajectories. The source strength was then taken from the lower panel of Fig. 2. From the same figure, the integrated mass flow during the April/May eruption is about 3 times the amount released in the days 14–18 April. This ratio and preliminary data by IES on the amount of tephra released during 14–18 April imply a total distal ash load of about 10 Tg to some 100 Tg during the whole eruption period.

2.3 Volcano plume identification from Meteosat SEVIRI data

In order to monitor the VA plume, the so-called dust image is a standard product used for visualization. This dust image is a red-green-blue (RGB) composite based on the brightness temperature differences between the 12 µm and 10.8 µm channel in red, the 10.8 µm and the 8.7 µm channel in green and the brightness temperature of the 10.8 µm channel in blue. This image allows not only identifying and tracking the ash cloud independent from daylight, but also indicates those regions, where the ash might be hidden due to ice on the dust particles or by clouds above. The time series of these images available every 15 min allows a very good judgment of the position (but not of altitude and density) of the ash cloud if correctly interpreted. However, such an interpretation is not possible from single images without further information, since the image sometimes exhibits weak contrast between ash and water clouds (see Sect. 3.4, Fig. 15 below). Therefore, we have developed a variant of this method for ash detection based on the Spinning Enhanced Visible and Infrared Imager (SEVIRI) Meteosat data.

It is well known that transparent ash clouds can be detected by evaluation of the brightness temperature (BT) difference of channels at 12 µm and 10 µm due to the

ACPD
10, 22131–22218, 2010

so-called reverse absorption effect (Prata and Grant, 2001; Prata, 2009). Usually the BT(10 µm)–BT(12 µm) is <0 K for ash particles and >0 for clouds, but atmospheric humidity, surface properties and the satellite viewing angle modify this threshold. For a refined ash product, the threshold was tuned to −1.0 K by visual judgment to provide a fair balance between a low false alarm rate and high detection efficiency. In a further step, the data was low-pass filtered in order to reduce the pixel noise inherent in the temperature difference data. As background we have chosen the BT(10.8 µm) grayscale image for better assessment of cloudiness in the meteorological situation. It has to be kept in mind, that the intensity of the ash product is not linearly related to ash concentration.

2.4 Flight planning

Flight planning at DLR was based on numerical weather forecasts, trajectory-based particle-dispersion models, satellite observations and ground based Lidar observations from many sources. The Falcon was operated as a "state aircraft" allowing for operations in otherwise closed air space. If necessary, the Falcon pilots were able to change the flight plan in-flight in direct contact with air traffic control.

In order to estimate the current and future spatial and temporal distribution of VA layers, the flight planning team relied on satellite products from Meteosat SEVIRI. In addition we used model predictions from various sources, including VAAC (http://www.metoffice.gov.uk/aviation/vaac/vaacuk_vag.html), the Lagrangian particle dispersion model FLEXPART (Stohl et al., 2005) of NILU (http://transport.nilu.no/browser/fpi), and calculations with the same model at DLR. Other VA forecasts like those from the EURAD model of the Rheinisches Institut für Umweltforschung, University of Cologne (http://db.eurad.uni-koeln.de/), from the COSMO-ART model of the Deutscher Wetterdienst (DWD, German Weather Service) and FLEXPART results from the Austrian Center for Meteorology and Geodynamics (ZAMG) in Vienna (http://www.zamg.ac.at/) were also available for some cases. Especially during the first days, the ash dispersion model predictions suffered from incomplete knowledge about the VA source strength.

ACPD
10, 22131–22218, 2010

Hence, the model results were mainly interpreted qualitatively to identify regions with high or low ash concentration. Later ground-based and in-situ observations allowed a better estimate of the source strength, and the model predictions provided increasingly reliable quantitative predictions of the VA mass concentration distribution.

A critical part of the flight planning process was the forecast of the expected (water) cloud cover to decide on whether the predicted ash plumes were embedded in clouds. The objective was to avoid measurements in VA plumes inside clouds, as Lidar signals are strongly attenuated in water clouds and the optical particle counters cannot easily distinguish between ash particles and water droplets. For this purpose, both VA prediction and weather prediction data were inspected simultaneously. Weather prediction was based on deterministic meteorological forecasts from the European Centre for Medium Range Weather Forecasts (ECMWF) and on COSMO-EU and COSMO-DE forecasts of DWD. For forecasting, we strongly built on experience gained in previous campaigns. For instance, refined versions of software used during a recent campaign (Voigt et al., 2010) were employed. For long distance flights, airports had to be selected for refueling which with high probability were free of VA impact.

When possible, the flight path of the Falcon was directed to pass over several ground-based Lidars: Munich-Maisach (48.21° N, 11.26° E, operated by the Meteorological Institute of the Ludwig-Maximilians University, MIM-LMU), Leipzig (51.35° N, 12.44° E; Institute of Tropospheric Research, IfT), Cabauw and Bilthoven, Netherlands (52° N, 5° E, Royal Netherlands Meteorological Institute, KNMI, and National Institute for Public Health and the Environment, RIVM), and Stuttgart (48.71° N, 9.21° E, Institute of Physics and Meteorology of the University Hohenheim).

After landing and cooling of the engines (minimum 2 h duration), the Falcon engines were inspected for ash deposit or damage visually and by using boroscopy (endoscopy with a 1.5 m flexible video sonde of 5 mm diameter). Moreover, samples of engine oil were analyzed in standard laboratories for sulfur content. On 20 April, several of the fuel injection nozzles in the combustion chamber of the Falcon engines showed corrosion damage slightly exceeding standard tolerance, because of erosion since last

ACPD
10, 22131–22218, 2010

replacement in July 2003. This needed to be repaired before the Falcon was ready to fly again. Inspection showed that the nozzle damages were not caused by the VA. The repair was performed within 3 days.

3 Results

3.1 Overview

In this section, we describe the observation results for eight missions, partly comprising several flights. Table 2 lists information on the 17 flights performed by the DLR Falcon research aircraft to survey and sample the emissions of the Eyjafjalla volcano on Iceland. The table includes takeoff/landing times and a short mission objective. A compilation of the flight tracks is shown in Fig. 3. Data from the instruments listed in Table 1 are available for all flights with following exceptions: Impactor sampling and SO_2 detector were not flown on the first flight. The GPaC instrument sampled large particles successfully only on 2 May 2010. The dew point hygrometer was only flown on 8 flights between 22 April and 3 May 2010. The 2D-C probe was added for all flights from 29 April onward.

From all flights, 35 flight legs were identified, when the Falcon was inside a VA plume. Table 3 lists 12 representative examples. These legs were selected based on increases in the particle concentration of coarse mode particles and SO_2 mixing ratio significantly above background. The Lidar signal was used to check whether a homogeneous ash layer was detectable. Moreover, the legs were checked for consistency of the computed backward trajectories with an ash source form the Eyjafjalla eruption. In fact, we excluded observations of aerosol traces measured over Leipzig at about 14:00 UTC 23 April, which may possibly result from other dust sources such the Taklimakan Desert in China (a possibility pointed out to us by Mike Fromm, personal communication). Most legs extend over about minutes to some tens of minutes. The variability of aerosol number concentrations over these times is considerable and about 100% (standard

ACPD
10, 22131–22218, 2010

deviation of the average). In all cases, the Falcon altitude information is derived from Global Positioning System (GPS) data. The results for 17 May, listed in Table 3 are the mean values over the descending and ascending legs over the North Sea within the altitude range of 3.2 to 6.3 km. The aerosol parameters reported in Table 3 refer to ambient pressure and temperature. The mass concentrations are computed as discussed below. All mass concentrations reported in the figures refer to "case N" (no absorption for FSSP). Besides leg-mean values, Table 3 also reports the maximum values of the 10-s mean values in these legs. Though not directly comparable, the maximum values are of interest because the VAAC reported maximum values, not mean values. Moreover, the ratio of maximum and mean values characterizes the scatter of the data. For analysis of CO and O_3 changes in the plumes, background concentrations are estimated from the data near the plumes; for SO_2, a constant background of 0.2 nmol mol^{-1} is assumed for this purpose. The relative humidity listed was measured with the Lyman-α-hygrometer. The CR-2 instrument results differ by less than 7% root-mean-square.

Table 3 lists also the effective diameter $D_{\text{eff}}=3V/(2A)$, i.e. the ratio between particle volume V and projected particle cross-section area A, each per unit ambient volume (Hansen and Travis, 1974; McFarquhar and Heymsfield, 1998). Here, V and A are computed by integrating over the respective size distributions from the accumulation mode and coarse mode particles (D>160 nm) assuming spherical particles. For ash particles of equal volume but spheroidal shapes and aspect ratio, e.g., 3:1, the effective diameter would be about 20% larger (Krotkov et al., 1999; Schumann et al., 2010).

Based on the Lidar signals, many of the VA layers show a multi-layer structure with two or even more layers separated by gaps of 100–300 m thickness with significant lower signal. The boundaries given in Table 3 refer to the maximum extent in case of multi-layers. The lowest mass concentrations were found during the flight on 9 May over Munich with an estimate of 2.5 µg m^{-3}. No clear VA layer could be identified from the Lidar measurements for this case. During the same flight on 9 May, a VA layer could be identified by the Lidar for which a mass concentration of larger 8 µg m^{-3} was

ACPD
10, 22131–22218, 2010

determined (Table 3). Thus, the detection limit for separated VA layers with enhanced aerosol backscatter is in the order of 8 µg m^{-3}.

3.2 Volcanic particle properties

Well loaded samples of VA particles suitable for single particle analysis were collected by the impactor-sampling devices inside the fuselage on 2 May and 17 May, legs 6 and 10 of Table 3. These samples were taken in VA clouds of different eruption periods and different plume ages over the North Atlantic (7–12 h age) and over the North Sea (60–84 h). GPaC samples are available for 2 May. The particles were collected on TEM (transmission electron microscopy) grids covered with formvar foil and adhesiv carbon substrate for electron microscopy. In the post-flight analysis, several hundred particles were investigated in a scanning electron microscope with an attached energy dispersive X-ray (EDX) detector. This analysis yields particle size, aspect ratio, morphology, and the element chemical composition for each single particle. Based on morphology, chemical composition and beam stability, the particles are assigned to one of the following groups: silicates, quartz, oxides, chlorides, phosphates, carbonates, sulfates, soot, biological, secondary, and mixtures of these groups. The particles consist of a mixture of ash particles and sulfuric acid droplets or sulfate particles. Figure 4 shows typical ash particles, with maximum size of 20 µm. Figure 5 shows sulfuric acid droplets and aggregates. Based on TEM studies (selected area electron diffraction) of the sample of both days, most particles are crystalline, i.e. no glasses.

The particles collected on the TEM grids of the impactors operated downstream of the aerosol inlet have sizes up to about 3 µm (equivalent projected area diameter). The mean aspect ratio is about 1.8 for particles smaller 500 nm and 2.3 for larger particles. The relative number abundance of the different particle groups is shown for the two sampling days in Fig. 6 as function of size. Below 500 nm, the aerosol is dominated on both days by secondary particles (ammonium sulfates/nitrates). For the larger particles, silicates and mixed particles are the most abundant groups (Fig. 4). The mixed particles mostly consist of silicates with small ammonium sulfate particles on their surface, which crystallized out of droplets (Fig. 5).

ACPD
10, 22131–22218, 2010

In both samples, most silicate grains (more than 90%) are mixtures of various minerals. Based on the chemical composition, the mixtures predominantly consist of feldspars, amphiboles/pyroxenes, and pure SiO_2 minerals (most likely quartz) in variable proportions. The composition of the silicates (external and within the mixtures) is different for the two sampling days (reflecting variable proportions of the different silicate minerals). For example, the Si/Al atomic ratio (±one-sigma standard deviation) decreases from 3.6±2.8 on 2 May to 2.8±1.2 on 17 May indicating an increasing feldspar component. The iron content is higher on 2 May with an atomic Fe/Si ratio of 0.33 compared to Fe/Si=0.08 for 17 May. The lower iron contents will lead to less absorption in the older plume. Furthermore, the sodium content is higher and the calcium concentration lower on 17 May.

The element chemical composition of the particles can be used to infer the complex index of refraction with an effective medium mixing rule (Ouimette and Flagan, 1982). Applying this mixing rule, the real and imaginary part of the refractive index is calculated as a linear combination of the refractive indices of the individual components weighted by their volume fraction. The refractive index of the individual components is taken from the literature, for details of the procedure refer to Kandler et al. (2009). As no further phase information on the specific iron minerals present in the volcanic dust is available, hematite is assumed to be the main absorbing component. The according refractive index data are taken from Sokolik and Toon (1999). The estimated uncertainties are 0.02 for the real part and possibly a factor of 3 for the imaginary part (Balkanski et al., 2007, estimate 0.04 and 50% for the real and imaginary part based on an extensive study for mineral dust).

Table 4 shows the calculated refractive indices at 630 nm and 2 µm (wavelengths of the FSSP and Lidar lasers) for 2 May and 17 May. While there is no variation between the two ash clouds for the particles smaller than 0.5 µm, consisting mainly of sulfates, a decreasing trend from 2 May to 17 May is visible for the larger particles, showing the composition change of the volcanic mineral dust. The highest values of light absorption are generally found between 0.5 and 1 µm in diameter, decreasing

ACPD
10, 22131–22218, 2010

towards larger particles sizes in the volcanic mineral dust fraction. Particles larger than 2 µm and up to 20 µm collected with the GPaC instrument in the wing station showed imaginary refractive index values of 0.001i with low variation. While on 2 May 40% of the particles had imaginary refractive index values at 630 nm wavelength smaller than 0.0005i, 47% between 0.0005i and 0.002i and 13% of greater than 0.002i, on 17 May 64% were weakly light-absorbing (<0.0005i), 29% were between 0.0005i and 0.002i and only 7% of the particles showed higher values of greater than 0.002i.

The mean particle density ρ_P derived from the relative number abundance of particle classes and published densities for the individual minerals (Tröger, 1982) is about 2.7 g cm^{-3}. The smaller particles with large sulfate content probably have a density similar to that of ammoniumsulfate (1.77 g cm^{-3}). We assumed ρ_P=2.6 g cm^{-3} to hold for all VA layers investigated in this study.

A particle size distribution is derived from the GPaC sample; see Fig. 7. For this purpose, all particles in an area of 0.14 mm^2 of the impaction plate were counted into size classes. From the cruise speed, sampling time and impaction area the sampling volume was determined. The resulting number size distribution was weighted with the collection efficiency at the given speed, determined by computational fluid dynamics (Kandler et al., 2010). However, as the GPaC was not fully extended out of its container in this case, the collection efficiency was most probably significantly lower than calculated. Therefore, the size distributions can only be regarded relatively.

3.3 Volcanic particle size distributions and mass concentrations

The particle size distributions are computed from the data of the optical sensors assuming two different particle refractive index values m, and a density value, ρ_P=2.6 g cm^{-3}. In this first analysis, we assume constant material properties (refractive index and density) for the entire size distribution analysis. The OPC and PCASP results are analyzed assuming absorbing particles, "case A", m=1.59+0.004i. The FSSP data are analyzed assuming either absorbing particles, "case A", or non-absorbing particles, "case N", with refractive index 1.59+0i. Table 3 lists the mass concentration results as obtained for these two refractive index values.

ACPD
10, 22131–22218, 2010

Figure 7 shows exemplary size distributions of number, surface area and volume for 19 April and 2 May, i.e. for cases with relatively low and high ash concentration. The results of the PCASP and OPC agree very well in the overlapping size range below approximately 1.5 µm particle diameter. Above this size, the FSSP data are selected to define the size distribution, while the sharp decrease of the OPC data reflects the decrease of particle penetration through the inlet with increasing particle sizes.

In case A, the particles controlling the total volume concentration and the integral over the volume size distribution occur in sizes of up to approx. 50 µm particle diameter (particles of 30 µm diameter contribute most to volume). As will be discussed further in Sect. 4.1, it appears unlikely that such large particles would survive long-range transport due to sedimentation. Furthermore, the measurements with the 2D-C probe with a lower detection size of about 25 µm at a flight speed of 120 m s^{-1} have not shown a single particle count in any of the VA layers measured in-situ with the Falcon. Therefore, we deem the size distribution for case A to deliver only an upper estimate for the total particle volume concentration. The results for case N provide a lower estimate, because the presence of at least some absorbing material follows from the chemical composition analysis and from the PSAP measurements for particles <2.5 µm. Larger particles appear to be less absorbing (Table 4).

We note that the total particle volume (mass) concentration is entirely dominated by the few largest size bins in the FSSP size range, no matter which refractive index is used in the inversion of the aerosol spectrometer data. This is due to the volume being controlled by the third power of the particle diameter and the number size distribution tailing off towards large particles remarkably slowly inside VA layers. This gives a volume size distribution having its maximum close to the upper margin of the entire size range covered by the instruments. For 2 May, in the lower-estimate case N, 65% of particle volume (mass) is residing above 10 µm, in case A it is even 90%. This implies that the derivation of the VA mass concentrations is entirely dependent on the FSSP measurements.

ACPD
10, 22131–22218, 2010

In this respect it is very important to note that the derived decrease of number concentrations and the increase in volume concentration with diameter is fully supported by the size distribution derived from the single particle analysis obtained with the GPaC on 2 May, see Fig. 7.

The largest uncertainty of the size spectra and mass concentration results comes from the large impact of absorption of laser light by the ash particles on the measured signal. As can be seen from Table 3, an increase of the imaginary part of the refractive index of the particles from 0 to 0.004 increases the analyzed ash mass concentration by about a factor of 2 to 7 in the individual cases, factor of 4 on average. In view of the fact, that the imaginary part itself is uncertain to a factor of about 3, this is the main uncertainty of this analysis. To estimate the impact of particle non-sphericity we assessed the instrument response of the FSSP by T-matrix calculations as explained above. Randomly oriented prolate spheroids provide the same amount of scattering for about 5–10% smaller area-equivalent diameter than spheres. However, for particles larger than 7 µm, and aspect ratios between 1 and 2, the computed particle size distribution was found to be far less sensitive to the particle shape than to the refractive index. An increase of the real part of the refractive index from 1.54 (as recommended for mineral dust, Balkanski et al., 2007) to 1.59 (a reasonable upper bound for VA according to Table 4) for non-absorbing particles, increases the derived mass concentration for selected legs (1, 6, and 10) by less than 15%. The sampling area of the FSSP is known only within an estimated uncertainty of 50%. It is adjusted in this study according to the overlap with the OPC/PCASP data for the cases inside VA layers, with low relative humidity (below 40%). The impact of particle hydration at these humidities is small (Strapp et al., 1992). The resulting uncertainty for the particle mass is about 40%.

ACPD
10, 22131–22218, 2010

3.4 Volcanic ash observations during individual flight missions

3.4.1 Aged volcanic ash layer in closed air space over Germany, 19 April

The first Falcon measurement flight for probing ash clouds from the Iceland Eyjafjalla volcano eruption was performed on 19 April 2010. The objective of this first flight was to assess the VA loading over Germany and the Netherlands at that time. The information was requested to support operational decisions on re-opening aviation operation over Germany after air space closure since the afternoon of 16 April.

Based on model predictions, we expected aged ash layers in the southern and middle part of Germany, with ash concentrations below those observed the days before. The ash was expected at altitudes below 6 km with rather inhomogeneous distribution over Central Europe, for this day. Figure 8 shows two FLEXPLART model simulations of the ash mass concentration for different model settings for the time of measurements. We see that the vertical distribution and the maximum values of the ash concentration were strongly dependent on the assumed model parameters, in particular on the source strength, particle sizes and sedimentation modeling. The maximum values of the ash near Leipzig in this case are incidentally smaller without sedimentation than with sedimentation. This is a consequence of different horizontal transport and shows the delicate sensitivity of transport to such detail: the trajectory analyses, Fig. 9, show that the VA air masses did arrive in Germany first on 16 April (originating from the first strong volcanic eruption on 14–15 April). The maximum mass concentration estimated from the Lidar observations over Leipzig and Munich reached about 1 mg m^{-3} on 16 April (Ansmann et al., 2010). The ash circulated thereafter around a high-pressure system over France before arriving in Germany a second time on 19 April. We note that the two backward trajectory models used (FLEXPART and HYSPLIT) provide age values, which differ by about 6% in this case, see Table 3. The residence time computed by FLEXPART in a particular grid cell is proportional to the contribution a source with unit strength in this cell would make to the mixing ratio at the receptor (Stohl et al., 2003). It is inversely related to the spread of the trajectories. The low spread and high

ACPD
10, 22131–22218, 2010

residence time over the volcano indicate strong ash uptake from the eruption plume over the volcano. For the ash layer over Leipzig at 4–5 km altitude, the ash was about 4.3–4.6 days old at the time of measurements. For a layer at 3 km altitude, a slightly shorter age was calculated (3.9–4.2 days).

As depicted in Fig. 10, the flight path of the Falcon was directed to pass over the ground-based Lidars in Munich-Maisach, Leipzig, Cabauw, and Stuttgart. The Falcon flew first at 8 km altitude, safely above the predicted VA layers. The layers were found at the position and time as expected from the model forecasts. The airborne Lidar detected several layers of strong backscatter indicating high particle concentrations at 3.7–5.8 km altitudes. Near Munich two elevated layers of 500–1000 m thickness were observed. Near Leipzig, these two layers were partly combined into one layer of 1.7 km thickness. In general, the ash layers were horizontally about 100–300 km wide. On smaller horizontal scales, the ash layers were more homogeneous than water or ice cloud layers. In the vertical, the layers were typically 0.5–2 km thick. Though clearly notable, the Lidar backscatter in the elevated layers (above 3.7 km) was lower than in the polluted boundary layer (below 3 km). Between Leipzig (north of 51.9° N) and Hamburg (south of 53.5° N) no elevated aerosol layers were observed. Under suitable viewing conditions (with the sun in the back), the ash layer was visible as a brownish layer to the observer, see photo, Fig. 11a.

The Falcon descended over Leipzig and probed the layers detected before by Lidar in-situ, first at 3.8–5.8 km altitude (at 15:08:35 to 15:15:35 UTC), and then at 2.2–3.2 km altitude (15:23:25 to 15:30:55). The Falcon did not descend lower. Hence, we cannot exclude additional ash layers to exist further down, see Fig. 12. During the descent over Leipzig, the in-situ measurements clearly revealed the presence of two ash layers. In both layers, the largest particle number concentrations were found at the smallest resolved particle diameters of about 10 nm. These particles likely originate from nucleation of sulfuric acid formed by oxidation of SO_2 emitted by the volcano (Fiedler et al., 2009; Jurkat et al., 2010). Comparably few particles were measured in the size range of about 3 to 25 µm, but they contributed most of the particle volume

ACPD
10, 22131–22218, 2010

and mass. There was no indication for the existence of larger particles beyond the size range of the FSSP (about 30 µm). Particles of such sizes are normally not present at these altitudes in the free troposphere. For example, in clean tropospheric air outside of the VA plumes and outside of clouds, the FSSP did not indicate the presence of any particles. Besides enhanced aerosol concentrations, the layers had high concentrations of CO, see Table 3, indicating VA layers. The measurements in the upper part of the boundary layer, which extended up to 3 km, showed considerable air pollution (more than 15 000 cm^3 fine particles; CO mixing ratio up to 200 nmol mol^{-1}). In addition, the number concentration of super-micron particles (>6.5 µm for case A, see Table 3) was enhanced. A large part of the high CO in the boundary layer was likely caused by urban pollution. The large super-micron particle concentration in that layer indicates also some contributions of volcanic aerosol to the boundary aerosol, which is confirmed by the ground-based Lidars (enhanced depolarization in the boundary layer; personal communication: A. Ansmann, V. Freudenthaler, 2010).

The size spectrum for the first flight leg above Leipzig was shown already in Fig. 7. The various particle measurement systems show consistency in the ambient volume and size-specific concentrations of volume, number, and surface of the particles for adjacent sizes. We see that the results depend strongly on the assumed refractive index of the particles. As explained before (Sect. 2.3), the analyzed particle sizes and the particle volume increases strongly with the imaginary part of the refractive index, accounting for laser light absorption. The number of particles is controlled by the Aitken mode, as expected. However, all particle sizes contribute about equally to the surface areas, and the particles with diameters of 15 or 25 µm, depending on the assumed refractive index, form the largest contribution to the specific volume. For larger particles, these spectra show a sudden drop in the volume concentration.

The mean particle mass concentration derived from these spectra for the upper ash plume over Leipzig (leg 1 in Table 3), is either 30 or 110 µg m^{-3} depending on the assumed limiting values of the index of refraction, N or A, respectively. The maximum values (10-s mean) reached up to 78 and 478 µg m^{-3}, respectively. The range is not

ACPD
10, 22131–22218, 2010

necessarily the largest possible range that could be derived considering all uncertainties of this analysis. The range reflects the values derived from integrating over the volume spectra for the two refractive index values. Because of sedimentation, see Sect. 4.1, the best estimate is likely near the lower value. For the lower layer, the particle mass concentration is estimated between 90 and 280 $\mu g\,m^{-3}$; this layer may contain some urban pollution.

Later in the flight, an ash layer was probed also at an altitude of 3.8 km near Stuttgart at about 17:20 UTC, see Table 3, leg 2. In the ash layer over Stuttgart, the aerosol properties were similar to those in leg 1 over Leipzig. The Stuttgart ash layer was also detected by Lidar (A. Behrendt, personal communication, 2010).

The concentrations of large particles measured in the VA on this day were comparable to concentrations measured typically in Saharan dust plumes (Weinzierl et al., 2009). We note that also the aerosol optical depth (0.4–0.6) of this case was comparable to values reported for Saharan dust.

The Falcon operated in the observed VA layers without any indication of technical problems. (The airports of Leipzig, Stuttgart and Munich were within range for emergency landing if that would have been needed.) The windows showed no visible ash traces. Silver foils attached to under-wing stations showed no visible impact from VA. Boroscopy of the Falcon engines showed no impact from the VA. The fact that the Falcon was operating without problems and the quantitative results with ash mass concentration below 0.2 $mg\,m^{-3}$ contributed to the decision to reopen air space over Central Europe on 21 April.

3.4.2 Mixed fresh and aged ash layers over Germany, Norway, and Poland, 22/23 April

A second mission, with three flights was performed on 22 and 23 April 2010, to test the validity of the VAAC predictions. The VA layer was predicted to move over the North Sea northeastwards. On 22 April, the Falcon was directed first to Hamburg, Germany, and after refueling from there over Denmark toward Southern Norway and

ACPD
10, 22131–22218, 2010

then back to Hamburg to observe possibly fresh VA layers near the southern coast of Norway. Because of predicted ash layers (by VAAC and FLEXPART), the return flight from Hamburg to Oberpfaffenhofen on 23 April was guided first eastbound over the Baltic Sea.

The VA distribution was quite complex during the flight from Hamburg to Norway and back. Two kinds of VA layers have been detected: 1) Along a flight path in east-west direction over the Skagerrak along the south coast of Norway, VA layers were found at altitudes between 2.2 and 6 km altitude embedded into cloudy areas, with high mixing ratios of SO_2 (up to 4 nmol mol^{-1}). The VA was rather fresh (36 h from backward trajectory analysis). One leg (leg 4 in Table 3) with high ash/SO_2 ratio (22 µg m^{-3}/1.8 nmol mol^{-1} at 19:10:35–19:12:55 UTC) was followed by another leg with low ratio (13 µg m^{-3}/2.8 nmol mol^{-1} at 19:14:15–19:17:45 UTC). 2) In addition, the Lidar detected an aged ash plume on the flight backward from Norway to Hamburg. This plume was about 1 km thick at altitudes up to 5.6 km in the northern part and decreased in altitude to 3.9 km with enhanced aerosol backscatter during the return flight towards Hamburg. The particle concentration was in general below the one measured over Germany on 19 April. The observations showed that the ash layers were found roughly at the same places and times as predicted, though details seem to differ by about 100 km in horizontal position.

3.4.3 Observations near the Volcano, Iceland, 29 April–3 May

The mission to Iceland was initiated on request of the Icelandic air traffic control agency (ISAVIA), because of frequent closure of the airport Keflavik, 40 km west of Reykjavik on Iceland. Keflavik airport is economically important for Iceland because it acts as a hub for the Iceland air fleet. The mission included five flights: from Oberpfaffenhofen to Edinburgh and from there to Keflavik on 29 April; a local flight over the volcano on 1 May; a flight with penetration into the upper parts of the VA plume over the North Atlantic and landing in Stornoway, Outer Hebrides, Scotland on 2 May; and a final return flight to Oberpfaffenhofen on 3 May.

ACPD
10, 22131–22218, 2010

On 29 April, the volcanic eruption was far lower than in the early eruption period. On arrival to Iceland, the plume was just visible as an enhanced cloud plume up to 3.9 km, i.e. about 600 m above a low-level cloud layer with 3.3 km cloud top altitude. This is consistent with the reduced activity depicted in Fig. 2. During descent to Keflavik, thin layers with very low VA traces were found at altitudes between 3.6 and 4.6 km, but nothing critical for flight safety. These results were important for local flight operations.

The flight on 1 May was the first highlight of the Iceland mission. The volcano was found to have again enhanced activity and it was clearly visible above the boundary layer clouds to the Falcon crew. The Falcon started from Keflavik and performed visual/photo and Lidar observations with flight path along and perpendicular to the mainly southeast plume direction, see Fig. 11b. The Falcon profiled first on the windward side of the plume and later again leeward but outside the plume. The ash concentration in the plume itself was obviously high and appeared far too high to allow in-situ measurements.

The ash plume appeared black, with some brownish color, far darker than in the aged plumes seen over Central Europe before. This could be an effect of dilution and ageing of the plumes when arriving over Central Europe but also due to different ash properties. It was noted that the ash was no longer in direct contact with glacier water as in the beginning of the eruption period.

At the volcano, the plume showed vigorous and intermittent convection, either due to intermittent eruptions or due to buoyancy. The crew felt enhanced turbulence in the air above the plume. At a distance of about 10 to 20 km, the plume became less vigorous and the initially apparently well-mixed plume spread laterally because of directional wind shear and possibly because of horizontally variable stratification similar to a cumulonimbus anvil (Lilly, 1988; Sparks et al., 1997).

Northwesterly winds prevailed (310 to 320 degree from 2 to 6 km altitude, based on the in-situ Falcon profiling near the volcano) with a small vertical directional shear, and with wind speed slightly increasing with plume altitude from about 10 to 30 m s^{-1} from 2 to 6 km altitude. From the Lidar wind profiling in 220 km distance, these values are

ACPD
10, 22131–22218, 2010

$10\,m\,s^{-1}$ at 2 km and $18\,m\,s^{-1}$ at 5 km altitude. The air temperature decreased from −4 °C to −25 °C over that altitude.

With increasing distance from the volcano, the plume top altitude first ascended from 3.5–3.8 (at the volcano location) to 5.1 km in about 20 km distance, and then varied between 4.7 and 4.9 km. At 220 km distance, 62.86° N, 15.50° W, on 11:49 UTC 1 May 2010, at a flight perpendicular to the plume axis, the plume had a width of about 35 km, top altitudes between 2.8 and 4.5 km, a depth of about 1.7 km, and a mean speed of about $14\,m\,s^{-1}$. Hence, the volume flux was about $0.8\,km^3\,s^{-1}$ with an uncertainty of $\pm 0.4\,km^3\,s^{-1}$. This result is of interest for plume dispersion modeling.

From the Lidar observations, it appears that the plume is rather well mixed with sharp gradients at the lateral and the upper boundary. A top-hat function appears more suited than a Gaussian profile to characterize the ash mass concentration inside the plume. There are also some indications that the large particles were sedimenting at the lower edge of the plume.

The Lidar was strong enough to penetrate the total plume layer. The plume was located above the planetary boundary layer topped with stratocumulus water clouds. Above the plume, and partly at the same altitude, thin cirrus was observed. The visibility of the boundary layer cloud below the plume indicates that the optical depth of the plume was about 1.5 at the 2.02 µm wavelength of the Lidar. Below the sedimenting ash, the boundary layer cloud layer was breaking up.

Outside the visible plume, the atmosphere showed no measurable traces of volcanic emissions. In agreement with the VAAC predictions, Keflavik airport was free of ash on this day. The report that the Volcano was more strongly active on 1 May than the days before caused an increase of the source estimate in the VAAC analyses for the following days (I. Lisk, personal communication, 2010).

The flight on 2 May was the second highlight of the Iceland mission. The Falcon started out of Keflavik and first passed again over the VA plume at distances of 37 and 158 km. At the volcano, the plume reached to about 4.2 km altitude, similar to the day before. From the volcano the Falcon headed south until 60° N latitude, where it turned

ACPD
10, 22131–22218, 2010

east crossing the plume at a flight altitude of about 6.7 km, and then returned first westward and then again eastward while descending slowly to perform in-situ measurements, see Fig. 13. The plume was found with the Lidar at altitudes between around 1.6 km and 3.8 km altitude, partly above, partly within maritime boundary layer clouds (cloud top at about 1.6 km). The Lidar signal indicated again broken cloud cover below the plume, possibly due to water uptake by acid-coated sedimenting particles.

The plume appeared less brown colored than on the day before, presumably because of dilution, sedimentation, and possibly wash-out of part of the plume particles. We note that the ash plume was below clouds during the day until shortly before the time of measurements as can be seen in pictures of the sensor MODIS on NASA's Aqua and Terra satellites (http://rapidfire.sci.gsfc.nasa.gov/gallery/?search=Eyjafjallajokull&date=). The lateral plume edges again appeared very sharp so that the crew decided not to enter the plume from the sides. Instead, the Falcon decreased speed (minimum 116 m s^{-1}) and descended down to 3.4 km altitude, about 200–400 m below plume top. The plume was entered at a distance of 450 km from the volcano, at about 7 to 12 h plume age (see Table 3). At the bottom of the plume, the ash was about twice that old because of lower wind speed

After entering the plume, all instruments showed strong increases of the measured values. The crew noted a darkening inside the cabin, and smelled increased SO_2 concentrations. Figure 14 shows the corresponding time series of aerosol and trace gas measurements. The signature of the ash plume is obvious in all parameters shown. However, due to the larger instrument's response time, the SO_2 signal is smoother and broader than the signal of the other instruments. Inside the plume, the number concentration of fine mode particles (10 nm–2.5 µm) increased by a factor of about 30, the number concentration of coarse mode particles (3–30 µm) increased from zero to 0.5 cm^{-3}, and the particle concentration in the accumulation mode increased up to two orders of magnitude. Obviously many fresh particles had been nucleated from sulfuric acid formed from SO_2. The Aitken mode showed maxima near the plume edges, indicating reduced nucleation in the plume center because of larger coarse-mode par-

ACPD
10, 22131–22218, 2010

ticle surface-area. SO_2 was strongly enhanced with measured maximum values of 150 nmol mol^{-1} (mean value 75 nmol mol^{-1}; background is about 0.2 nmol mol^{-1}). The actual maximum value may be larger because of the instruments inertia. Furthermore, CO was enhanced (110 to 280 nmol mol^{-1}), and O_3 was reduced (10–60 nmol mol^{-1}) with a strong anti-correlation of the two signals. The reduced O_3 indicates ozone loss possibly by halogen chemistry or heterogeneous chemistry (Bonasoni et al., 2004; von Glasow, 2010). The two humidity sensors give consistent results (differences are due to different response times). In the lowest part of the flight in the plume, the relative humidity reached a minimum of only 45%. The reduced relative humidity may be either caused by uptake of water by the aerosol together with sedimentation of the heavier water-loaden particles, or by a sinking of the air masses at the boundary of the high-pressure system with adiabatic warming of the air mass for constant water mixing ratio.

After about 30 s of measurements inside the plume, the crew signaled to the pilots to leave the plume. This decision was made mainly because of strongly enhanced light absorption by the ash aerosol (indicated by the 3-λ-PSAP) and increasing SO_2 concentration. The Falcon slowly ascended avoiding overpowering the engines. After nearly 3 min the Falcon was back in clear air. It then continued flight and arrived after about one flight hour in Stornoway on the Outer Hebrides, Scotland. The next day, boroscopy and visual inspections showed no damages to the aircraft. Hence, the Falcon returned without further notable VA penetrations back to Oberpfaffenhofen on 3 May.

During the 3-min ash plume penetration, the mean ash mass concentration ranged from 0.2 to 0.9 mg m^{-3}. The maximum values of the 10-s mean data reached up to 0.55 and 2.6 mg m^{-3}. In this case, we take as best estimate the arithmetic mean value of the two mean values for cases N and A. This may be justified, because this fresh plume appeared very dark, and hence contains absorbing material, and particles larger 20 µm were collected on the GPaC particle collector. The effective diameter from the particle size distribution is near 7 (4–10) µm. Hence, still quite large particles were detected, even 200–400 m below plume top and at distance of 450 km from the volcano.

ACPD
10, 22131–22218, 2010

Based on the observations, one can again compute the plume volume flux and in addition the ash mass flux, from $F = xyvc$. Here the horizontal extent is x=61 (56–65) km, the vertical extent is y=1.3 (1.3–2) km, the wind speed in plume direction, assumed perpendicular to the flight path, is about v=11 (11–14) m s^{-1} on average over the plume. These values imply a plume volume flux of 0.9 (0.8–1.8) km^3 s^{-1}. This value is only slightly larger than the day before, indicating weak mixing of the plume with ambient air. The mass concentration c is assumed to be 0.5 (0.2–0.8) mg m^{-3}. Hence, the mass flux is about 440 kg s^{-1} (range 160–1500 kg s^{-1}). This value is a lower limit for the total mass flux because larger concentrations of larger particles are to be expected in the lower part of the plume. From an estimate of the Lidar backscatter, a factor of 2–4 higher concentrations can be expected within the plume. Taking a value of 2 mg m^{-3}, the mass flux could be about 1800 kg s^{-1}. A value of 3000 kg s^{-1} with a range from 1000–10000 kg s^{-1} was reported to the VAAC on 4 May.

It should be noted that the volcano was only moderately active during the 1–2 May period. Based on Fig. 2, a factor 50 larger eruption rate could be realistic for the maximum eruption period of 14 April. Hence, we may speculate that the mass flux in the distal plume at ages of order 10 h may have reached up to 90 Mg s^{-1} during the April/May 2010 Eyjafjalla eruption period. In order to convert this mass flux into total mass during the eruption period, we refer to Fig. 2. Form that figure (see also Table 3) we take a mass flow rate of 2 units during May 2. The integral over the whole period is 6000 h units. Hence, the total mass flux is 3000 h times the instantaneous mass flux of 1800 kg s^{-1} at 2 May. Hence, the volcano ejected about 40 Tg of ash mass for the whole April/May 2010 eruption period. Of course, this is not more than an order of magnitude estimate.

The measured mean SO_2 mass concentration (142 µg m^{-3} for 75 nmol mol^{-1} at the measured ambient conditions, see Table 3) is about 3.5 times lower than the ash mass concentration (0.5 mg m^{-3}). Hence, we estimate the SO_2 mass flux rate to be of the order of 500 kg s^{-1} on 2 May, maximum of 25 Mg s^{-1} at the beginning of the eruption period, and about 10 Tg for the whole April/May 2010 period.

ACPD
10, 22131–22218, 2010

3.4.4 Less ash than predicted, South Germany, 9 May

On 9 May, an air mass with some ash content arrived in Southern Germany after 6 days of transport from the volcano southward over the North Atlantic and then over Northern Spain, Southern France, Switzerland or Western Austria, to Southern Germany. Satellite observations had shown ash signals over the North Atlantic but no indications for significant ash concentrations on its way from Spain to Germany. A flight of the Swiss MetAir-Dimona aircraft, a two seated, powered glider (http://www.metair.ch/; B. Neininger, personal communication, 2010) did not find indications for VA at altitudes up to 4.5 km. The VAAC products indicated a few small spots over Southern Germany with ash concentration exceeding 2 mg m^{-3}. With 60 nautical miles added to account for uncertainty ranges, these predictions caused the airports of Munich and Stuttgart to close at 13:00 UTC. At the beginning of the closure, a VA layer of about 1 km thickness became visible at altitude of about 4 km in the ground based Lidar observations at Munich-Maisach. At about 14:00 UTC, the Falcon started and performed in-situ measurements profiling over Munich, then flew at larger altitudes toward Stuttgart and Leipzig, and spiraled again near Bayreuth and Munich. The ash mass concentrations measured during that flight were below 18 µg m^{-3}. In view of these data and changed VAAC evening predictions, the airports opened again at 19:00 UTC, two hours earlier than planned in the afternoon.

3.4.5 Multiple thin layers, South-West North Sea, 13 May

The measurements of this day were triggered by Meteosat dust image observations of 11 May, indicating that a part of the ash cloud has left the area forecasted by the VAAC due to a mesoscale disturbance west of Ireland. On 12 May, this part of the ash cloud was observed over Northern France and Southern England. The ash layer was predicted by the FLEXPART tracer model but not identified as critical for aviation (> 0.2 mg m^{-3}) by the VAAC. For air traffic reasons, the flight, which was planned for 12 May, had to be postponed to 13 May.

ACPD
10, 22131–22218, 2010

During the flight on 13 May, the ash cloud was detected over the North Sea at the Northern end of the English Channel. The situation was not simple: Plumes with different microphysical and chemical properties were found. The SO_2 plume was separated from the plume with largest particles, presumably because of sedimentation effects. The photographs showed different layers at different altitudes, see Fig. 11c. The ash layer had a depth of 400 to 700 m and was inclined (2800–3300 m over the channel and 5000–5400 m over the Norwich area further north). The plume was forecasted at altitudes between 3 and 5 km. The measured location of the plume coincided with the forecast (FLEXPART) position of the plume. The maximum ash concentration along the flight path was less than 42 $\mu g\,m^{-3}$. The maximum was observed at 5.2 km altitude at 53.5° N, 1.4° E, at 14:10 UTC, with enhanced concentration of particles larger ~80 nm and enhanced absorption coefficient. The layer contained SO_2 at concentrations up to 25 $nmol\,mol^{-1}$ (mean 9.7 $nmol\,mol^{-1}$), far above instrument background (0.2 $nmol\,mol^{-1}$). The region with high SO_2 and large particles was rather humid (50–60%). Drier conditions prevailed further North, at 3–7 km altitude, containing smaller particle VA remainders without SO_2, apparently in a different kind of air mass.

3.4.6 Strong fresh VA plume arrival over England, 16 May

On 14 May, the VAAC predicted a strong VA layer, potentially affecting European air space. This ash layer was traced from the British Islands to the Alps in the following days with three Falcon flights and other observations. The Falcon was requested to fly first on 16 May and later on 17 and 18 May, in order to assess the predicted ash distribution. Hence, this was the start of a Lagrangian experiment.

The ash cloud front was expected to arrive in Ireland and England on Sunday morning (16 May), first at low and later at upper tropospheric levels traveling quickly within two days up to Germany and possibly further. The predictions, see Fig. 15, implied a possible closure of large fractions of the northern part of the Central European air space. The VA layer arrived at the northern edge of Scotland and western coast of Ireland in the late evening of 15 May. This was first indicated by ground-based observations at Mace Head (53.3° N, 9.9° W), showing a sudden increase in sulfate con-

ACPD
10, 22131–22218, 2010

centrations. The Lidar at this station showed a subsiding plume (C. O'Dowd, personal communication, 2010). The enhanced sulfate signal ended after a few hours indicating that Mace Head was touched by the southern most edge of the ash plume only shortly. The CARIBIC aircraft detected enhanced SO_2 columns by differential optical absorption spectroscopy (Heue et al., 2010) below 7 km altitude over Northern Ireland, 55° N, 7° W, 09:00 UTC 16 May (K.-P. Heue, personal communication, 2010). The predictions for 12:00 UTC 15 May indicated strong cloud cover over Southeast England (near London), but no high level clouds and only scattered mid level clouds were predicted over the Irish Sea.

When the Falcon reached the Irish Sea near 54.2° N, 4.5° W at 13:26 UTC, the Meteosat ash product indicated that the ash plume was located further north and was moving eastward more quickly than predicted, see Fig. 15. Therefore, the Falcon was directed northeast. Immediately after changing the flight route, the Lidar detected a thick ash plume at altitudes between 3.6 km and 7 km at 54.7° N 3° W, while the Falcon was flying in ash-free air masses at 7.2 km altitude. At 54.8° N, 0.2° W, 6 km altitude, at 14:10 UTC, after extensive Lidar observations, the Falcon performed in-situ measurements in the upper most edge of the VA plume. The measurements showed many large particles, with a mean mass concentration of about 15 to 53 $\mu g\,m^{-3}$; 10-s maximum ash concentrations up to 330 $\mu g\,m^{-3}$ in case A (see Table 3); a maximum SO_2 concentration exceeding 30 $nmol\,mol^{-1}$; and the ash plume was clearly visible as a grey-black layer. The ash plume was clearly located in the Meteosat ash product; see Fig. 15. As noted before the ash product is not a linear function of the vertically integrated ash concentration. The VAAC product shows the maximum ash concentration expected in the 6-km vertical layer. The observations confirmed the existence of a high concentration VA plume, roughly as predicted by the VAAC, but 100 to 200 km further north. The horizontal displacement between the plume predicted by the VAAC and the plume visible in the satellite image could be caused by wind field errors in the model driving the NAME model or by vertical wind shear and errors in the plume altitude assumed for these predictions.

ACPD
10, 22131–22218, 2010

3.4.7 One hour of measurements in ash over the Southern North Sea, 17 May

The plume observed over Northern England was predicted to travel further eastward and reach Germany the next day, see Fig. 16. Therefore, the Falcon performed two measurement flights, first over the Baltic Sea and East Germany, and then over the Netherlands and the North Sea, with vertical profiles between about 6 and 1.5 km altitude. At the same time, VA layers were observed at 2–4 km altitude by a ceilometer over Essen (51.4° N, 7.0° E) in Northwest Germany (H. Flentje, personal communication, 2010). Over Leipzig, the VA layer was visible between 2.5 and 3.5 km altitude according to the Lidar depolarization signal at 12:00 UTC (Albert Ansmann, personal communication). During the flight, the Meteosat ash product revealed the maximum ash concentration at 2.5° E, 54° N at 13:00 UTC, moving southwards to 2.5° E, 53° N at 16:00 UTC, i.e. further west than predicted. The VA layer was detectable also in the visible range of Meteosat SEVIRI. This information was used to direct the Falcon to fly further out to the North Sea, where an ash cloud was clearly visible, see Fig. 11d. As seen in the Meteosat ash product, Fig. 16, the measured plume arrived over The Netherlands the same day at about 18:00 UTC. The Cabauw Lidar detected the ash layer at 5 to 7 km altitude at 19:30 UTC (Keith Wilson, personal communication).

The Lidar observations revealed a clearly detectable VA plume at 3.2 to 6.3 km altitude over the North Sea area, see Fig, 17. The backward trajectory analyses showed that this layer contained ashes of various ages; about 60 h at layer top, 80 h at layer bottom, because of different wind speeds. In the plume, an average mass concentration in the order of 0.18 to 0.74 mg m^{-3} is estimated from the in-situ measurements (the lower value is more likely, see Sect. 4.1). Mass concentrations derived for case N, see Fig. 18, reached up to 0.5 mg m^{-3} and SO_2 mixing ratios were up to 66 nmol mol^{-1} (based on 10-s averages). The aerosol measurements showed a thick ash layer with highly elevated particle concentrations in all size classes. Obviously, the SO_2 correlated well with the measured particle concentrations. The one-hour layer-mean SO_2 concentration of 27 nmol mol^{-1} in a layer between 3.6 and 6.3 km altitude corresponds to about 4.2 Dobson units (1 DU=2.7×10^{16} cm^{-2}).

ACPD
10, 22131–22218, 2010

3.4.8 Decreasing ash load of ageing plume over Germany, 18 May

During 18 May, the plume reached Southern Germany and the Alps. At 00:00 UTC 18 May, the VAAC predicted a "black zone" with ash concentration exceeding 2 mg m^{-3} over the Netherlands for 12:00 UTC 18 May. Six hours later, the predictions, see Fig. 19, showed lower ash concentrations over the Netherlands but suggested a possible airport closure for a small band over Northern Germany along the river Ems, affecting the airports of Emden and Münster, possibly starting 12:00 UTC 18 May. This was supported by computations with the COSMO-ART model of the DWD and Karlsruhe Institute of Technology (B. Vogel, personal communication, 2010). However, the Meteosat ash product of 03:30 UTC 18 May showed the VA maximum further west, at about 48° N, 7° W, see also Fig. 19. Therefore, a further Falcon flight was performed to check for the ash cloud loading. After the Falcon had started, at 09:00 UTC, the German Civil Aviation Authority (DFS) informed that no airspace closure was foreseen over Germany that day.

The ash plume was detected over West Germany by Lidar in Jülich during the night, but a cloud layer stopped the measurements at around 06:30 UTC (M. Krämer, personal communication, 2010). An ash cloud and a layer of sulfuric acid droplets arrived in low concentrations near 600 hPa and 450 hPa above Zurich (47.5° N, 8.5° E) at about 00:00 UTC 18 May (T. Peter, personal communication, 2010). At 07:00 UTC, the DWD reported ash layers to be observed with Ceilometers over Western Germany (Essen) with maximum ash concentration estimated to exceed 100 µg m^{-3}. Rising SO_2 levels above 2 nmol mol^{-1} at the Schneefernerhaus station (47.4° N, 11.0° E) indicated arrival of VA in Southern Germany (H. Flentje, personal communication, 2010). The Stuttgart Lidar reported VA between 3.0 and 4.5 km altitude at 07:40–08:00 UTC (A. Behrendt, personal communication, 2010). At 10:00 UTC, the DWD reported VA layers between 2 and 6 km altitude, mainly over the western and southern parts of Germany. The VA mass concentrations were estimated from DWD Ceilometer signals to reach up to 80–200 µg/m^3 in the thicker layers, and the DWD ozone profiling of Hohenpeis-

ACPD
10, 22131–22218, 2010

senberg (47.8° N, 11.1° E) indicated an ash cloud at about 4 km altitude (H. Flentje, personal communication, 2010). DWD Lidar backscatter signals over Lindenberg (52.2° N, 14.1° E) at 3–7 km altitude were interpreted as cirrus or other clouds; no VA traces were reported until 12:30 UTC (F. Immler, personal communication, 2010). Measurements with a GRIMM dust monitor (15 aerosol sizes between 0.3 and 20 µm) by the Swiss aircraft over Switzerland revealed a shallow layer with VA above 3.5 km, first above Bienne (47° N, 7° E) at 12:00–14:00 UTC; the maximum VA mass concentration was estimated near 0.25 mg m^{-3}; the team also detected increased CO_2, CO, reduced O_3, and reduced H_2O (B. Neininger et al., personal communication, 2010).

The Falcon performed a flight over Germany and the North Sea 07:25–10:34 UTC 18 May. Almost over the entire Falcon flight, multiple VA layers were observed over Germany by the Falcon Lidar. In a layer over Hamburg, the maximum SO_2 mixing ratio reached up to 25 nmol mol^{-1}, the aerosol mass concentrations exceeded 55 µg m^{-3}. During the return flight, in-situ flight legs were flown in Southern Germany between 3.5 and 5.2 km altitude. During descent between Stuttgart and Munich, this ash plume showed the highest concentration during this flight with 10-s mean values up to 0.36 mg m^{-3} for analysis N. The results are consistent with Meteosat ash products, showing dispersed ash traces over Germany between 06:00 and 11:00 UTC 18 May 2010; see Fig. 19. As a whole, the ash clouds were diluted and mass concentrations were lower than over the North Sea area on the previous day.

4 Discussion

4.1 Ash mass concentration properties

As has been pointed out before, it is not possible to measure the ash mass concentration directly. Instead, we derive the ash mass concentration by integration over the volume size distribution deduced from the optical particle counters. We recall that the results of this method depend strongly on the assumed refractive index, in particular the imaginary part, particle bulk mass density and to lesser extent, on the particle shape.

ACPD
10, 22131–22218, 2010

Practically all size distributions measured exhibit maximum volume contribution for the largest particles counted. Similar findings were reported from other in-situ and remote sensing studies, without further explanation, for volcanic ash (Hobbs et al., 1982, 1991; Watson and Oppenheimer, 2001), and desert dust (Duce, 1995; Weinzierl et al., 2009).

We explain this result with the effect of sedimentation in a finite and vertically nearly homogeneous ash layer; see Fig. 20. We assume that the measurements occur at a certain level z_m with distance s below the ash-cloud top z_t. In the young plume, those particles, which get lost by sedimentation, are replaced by particles of the same size D from above. However, after some time s/v depending on the distance s and the fall velocity $v(D)$, which increases quadratically with diameter D, the layer above the level of measurements is depleted from all such large particles (see Fig. 20, left panel for $t>t_0$). Thereafter, particles falling down are no longer replaced by particles coming from above and then this size class is depleted. This depletion of particles progresses with plume age t, see right panel of Fig. 20. It starts in the largest size class and then gradually affects smaller ones. Therefore, after some plume age t, the volume-size distribution still increases with diameter up to a peak maximum. However, the volume concentration vanishes above the size D for which $t>s/v$. Near the volcano, tephra samples from the ground (see Sect. 1) indicate initial peak diameters D_{max} of 60–150 µm. The value of D_{max} is far larger than maximum particle sizes detected in the airborne measurements. Hence, all our results occur at times when particles larger than this initial peak size have been lost. If the plume particle distribution is vertically inhomogeneous within the layer, the volume concentration is changed also below the cut-off at earlier times so that the cut-off becomes somewhat smoothed. Turbulent motions may also transport larger particles upwards and will further contribute to smooth the size distribution. In order to be comparable to the sedimentation velocity, the vertical turbulent velocities must be larger than 0.1 m s^{-1} for particle sizes larger than 30 µm. Horizontal mixing with ash-free air outside the plume will reduce the concentrations at all sizes. Hence, the observed behavior of the volume-size distributions appears to be reasonable.

ACPD
10, 22131–22218, 2010

Next, we ask whether the measured particle sizes are realistic in magnitude. Because of sedimentation, very large particles would fall below the altitude at which the measurements are performed. Neglecting rarefied gas effects and non-sphericity of the particles, the classical Stokes law (Hinds, 1999) relates the terminal fall velocity v to the particle diameter D, gravity g=9.81 m s^{-2}, particle bulk density ρ_P=2.6 g cm^{-3}, and dynamic viscosity of air η=14×10^{-6} kg m^{-1} s^{-1},

$$v = \frac{g\rho_P D^2}{18\eta} . \quad (2)$$

The fall distance over plume age t_{age} is s=vt_{age}. Hence, the maximum particle size D_{max} surviving sedimentation at an altitude s below the initial plume top altitude is about

$$D_{max} = \sqrt{\frac{18\eta s}{g\rho_P t_{age}}} . \quad (3)$$

Inclusion of a shape factor (Hinds, 1999) would increase the values of D_{max} by about 10 to 30%, which is not essential for this discussion. Figure 21 shows the limiting diameter D_{max} as a function of age for typical fall distances s of up to 6 km. Since the plume top height was mostly below 10 km and most of the measurements were performed at 2.6 to 6.5 km, this range should cover all measured cases. The special case of 2 May, with smallest fall distance (0.2–0.4 km) and smallest plume age (about 0.3 d), is plotted also. Because of unknown vertical synoptic motions, the fall distance is different from the distance to the actual plume top altitude, and we cannot constrain this fall height further, therefore. Hence, plumes of ages larger than 2 days should be free of particles larger than 15 µm due to sedimentation.

The analysis of the FSSP data with refractive index 1.59+0.004i (case A) shows significant volume contributions at particle diameters up to 50 µm, whereas for the limiting case N (1.59+0i) the diameters stay below 30 µm. Even the effective diameter D_{eff}, which is typically 2 to 5 times smaller than the maximum particle size, seems to

ACPD
10, 22131–22218, 2010

exceed the limiting curves when analyzed for absorbing particles (A), but stays well below these limits for non-absorbing material (N); see Fig. 21.

For these reasons, we conclude that the imaginary part of the refractive index is significantly less than 0.004, at least for the aged plume. Therefore, the best estimate values for plume ages larger one day are likely those derived for case N. This is in agreement with the chemical analysis of particle samples that show lower absorption for 17 May than 2 May; and lower absorption for larger particle sizes (see Table 4). However the plume of 2 May, with smallest age (0.3 d), darkest color, stronger absorption (Table 4), and larger particles with 20 µm diameter collected with the GPaC, see Fig. 4, are consistent also with more strongly absorbing ash particles (case A).

4.2 Ash mass and trace gas correlations versus plume age

For aviation safety, it would be desirable to have a parameter indicating volcanic emissions that is more easily measurable than the ash mass concentration. Volcanoes are a major source of SO_2 in the atmosphere (Bandy et al., 1982; Hobbs et al., 1982, 1991; Hunton et al., 2005). However, there are documented cases where ash and SO_2 separate and travel in different heights in the atmosphere (Prata, 2009). In fact, we too found cases with enhanced ash concentration but virtual no SO_2 and vice versa (e.g. on 22 April over the Skagerrak and on 13 May over the North Sea). Such separation can be due to particle sedimentation or result from photochemistry and washout. Moreover, the ratio of SO_2 to ash concentration likely varies between different volcanoes and eruption periods. Nevertheless, our measurements show a weak correlation between the SO_2 and the ash mass concentration (see Fig. 22). In logarithmic scales (not plotted), one notes that the correlation is better at higher concentrations (fresh ash plumes). This correlation might be of practical value for rough estimates of ash mass concentration for given SO_2 measurements. The latter measurement is far simpler than that of the ash mass.

For this specific volcano and the eruption in April/May 2010, an ash concentration of 1 mg m^{-3} corresponds to about 200 nmol mol^{-1} SO_2 enhancement in mixing ratio.

ACPD
10, 22131–22218, 2010

Hunton et al. (2005) also show a correlation between aerosol volume and SO_2 mixing ratio. Their results correspond to only 0.044 mg m^{-3} increase in aerosol mass for an SO_2 enhancement of 200 nmol mol^{-1}, because their particle counters measured only particles smaller than 2 µm. For CO enhancement we also find quite large increases inside volcanic plumes (about 140 nmol mol^{-1} in CO for 1 mg m^{-3} of ash mass), at least for young plumes, but the correlation is weaker, and the larger background (order 100 nmol mol^{-1}) and its larger variability makes CO less suited for VA detection.

The data points in Fig. 22 for 2 May, with the smallest plume age, appear as outliers, with far larger SO_2 and CO concentrations relative to the ash mass than for the cases with larger plume ages. The difference could be caused by a still larger SO_2 and CO content in the young plume, which is reduced in older plumes by oxidation (though the chemical time scales for CO and SO_2 are different). Alternatively, this suggests an underestimate of the ash mass concentration in this case. In fact, allowing the young ash particles to be more absorbing than the older ones, would bring this point to larger ash mass values and hence closer to the correlation line. Another explanation could be that the Falcon measured only in the upper-most part of the plume, in which the concentration of the large particles is lower due to sedimentation than in the lower part of the plume.

Another simple ash concentration indicator is plume age. In general, one would expect that the concentrations decay with plume age, mainly because of dilution, and in fact, this is generally the case. However, the details depend strongly on the actual volcano source strength feeding the plumes measured and on the meteorological conditions, as to be expected. For example, the absolute particle concentration was rather modest in the youngest case, over the North Atlantic (2 May) because at the time of leaving the volcano the eruption source strength was well below maximum values. In order to reduce the influence of source strength, we normalize the measured data with the source strength derived from Fig. 2 at the time of emission at the volcano as computed with the HYSPLIT backward trajectories, see Table 3.

ACPD
10, 22131–22218, 2010

Figure 23 shows the concentrations normalized to source strength of 100 units (the maximum value in the complete period, see Fig. 2) versus plume age. We note that the concentrations follow roughly an exponential decay law with half times of order 20 to 22 h. The time scale for ash is larger than expected, that for SO_2 appears to be smaller than expected previously (Prata, 2009). Still, the correlation is quite weak, mainly because of the strong influence of the specific meteorological conditions. Moreover, this result applies to the Eyjafjalla only and only for the period April/May 2010. Other decay laws will apply for other volcanoes and other periods.

4.3 Effective diameter

The effective diameter, defined in Sect. 3.1, is useful for relating the extinction coefficient (optical depth) of aerosol layers to the ash mass concentration (ash mass path) when the extinction efficiency is approximately constant (Hansen and Travis, 1974; Schumann et al., 2010). In the data, the coarse ash particles contribute most to the volume while the accumulation mode particles often contribute most to the cross-section area. Inclusion of the area of the smaller Aitken mode particles (with negligible volume) would give even smaller values of D_{eff}.

Values of D_{eff}, derived from the FSSP data for absorbing and non-absorbing particles, are listed in Table 3. Here we discuss the results for analysis N. The values vary between 0.4–5 µm, and D_{eff} increases less than linear (about power 0.5) with the ash mass concentration, but with large scatter; see Fig. 24. The magnitude of the D_{eff} values is similar to the values 1–3 µm derived from multi-spectral optical depth analysis for the Mt. Etna aerosol plume (Watson and Oppenheimer, 2001). The large scatter of the relationship between D_{eff} and the mass concentration implies large scatter in the extinction coefficient of light. This fact could complicate Lidar analysis of mass concentrations (Ansmann et al., 2010; Flentje et al., 2010). The extinction coefficient ε and the mass absorption coefficient k are $\varepsilon=(3/2)Q_{\mathrm{ext}}c/(\rho_{\mathrm{P}}D_{\mathrm{eff}})$ and $k=(3/2)Q_{\mathrm{ext}}/(\rho_{\mathrm{P}}D_{\mathrm{eff}})$, for given particle density ρ_{P}, and ash mass concentration c. The extinction efficiency Q_{ext} would be about 2 in the geometric optics limit (Hansen and Travis, 1974). The data show

ACPD
10, 22131–22218, 2010

that the mass extinction coefficient (of order k=0.3 to 2 $m^2\,g^{-1}$) decreases with the ash mass concentration. The values of ε are of order 300±100 Mm^{-1} for c=1000 $\mu g\,m^{-3}$. This value of ε is not much different from the range of values (400–600 Mm^{-1}) deduced by Ansmann et al. (2010) from Lidar data for Leipzig on 16 April 2010. Both ε and k increase when taking the cross-section area and variable scattering efficiency of the smaller Aitken particles into account. This should be the topic of a future study.

5 Conclusions

Airborne measurements have been performed in VA plumes over Europe between Southern Germany and Iceland during the major eruption period of the Eyjafjalla volcano in April/May, 2010. The measurements provided information on the ash plume properties in many respect, in particular the particle properties, the spatial distribution, horizontal and vertical depth, Lidar backscatter, particle number-size distribution, mass concentration, mixing ratios of some trace gases (CO, SO_2, O_3), and meteorological parameter values including wind profile and relative humidity.

The combination of remote sensing profiling with Lidar and in-situ measurements of aerosol and trace gas in-situ instruments including particle impactor-sampling turned out to be well suited for this purpose. Lidar observations from above served as pathfinder before the aircraft descended into ash plume layers. The Falcon aircraft being equipped with Lidar windows and wing stations to carry optical particle counters to measure large ash particles was essential for this purpose. Weather and ash plume forecasts and refined satellite observations were essential for flight planning. During analysis, trajectory models were used to identify the plume age, the initial plume release height at the volcano, and the relative eruption source strength. The latter was used for normalization when comparing ash and trace gas concentrations at various plume ages.

Particle counters inside the cabin see only particles with diameters smaller than about 2.5 to 1.5 µm (decreasing with altitude) because of losses in the aerosol inlet,

ACPD
10, 22131–22218, 2010

and hence often underestimate the ash concentration considerably. The analysis of the ash mass concentration and the effective diameter from the suite of instruments for optically counting and sizing the particles is highly sensitive to the refractive index and material mass density derived from particle elemental composition analysis with scanning electron microscopy. Analysis of particles collected by impactors revealed particles up to 20 µm at about 10 h plume age, with size dependent composition, refractive index, and density properties. Ash mass concentration is evaluated for a material density of 2.6 g cm^{-3} and either non-absorbing or absorbing particles (refractive index 1.59 or 1.59+0.004i). In the absorbing case, the ash concentration is about a factor of four larger than in the non-absorbing limit. Consequently, the ash mass concentration is typically uncertain to a factor of about four. Based on the chemical composition analysis of single particle of various sizes and because of sedimentation constraints for aged plumes, the smaller (non-absorbing) results seem to be the more realistic ones. Future quantitative revision of the reported ash mass concentration results is still possible, in particular when more constraints on the optical particle properties become available.

The VA cloud spread over large parts of Central Europe, mostly in layers of a few 100 m to 3 km depth, at 1 to 7 km altitude, and typically 100 to 300 km width. In many cases, the ash plume was several days old, with concentrations below 0.2 mg m^{-3}. The ash was detectable to the combined Lidar/in-situ measurements in regions with predicted ash clouds, even at very low concentrations of order 0.01 mg m^{-3}. In selected cases, the Falcon flew in ash clouds up to about 1 mg m^{-3} for a few minutes and in an ash cloud of about 0.2 mg m^{-3} mean concentration for about one hour (maximum larger than 0.46 mg m^{-3}). The SO_2 concentration in young plumes is correlated with the ash mass concentration. Typically, 0.5 mg m^{-3} ash concentration is related to 100 nmol mol^{-1} SO_2 mixing ratio, and 70 nmol mol^{-1} CO mixing ratio increases above background. However, other correlations will apply for other volcanoes and other periods. In aged ash layers we found enhanced ash concentration but virtual no SO_2 and vice versa. Under suitable daytime conditions, the ash plume was visible to the crew as faint dark layers even for low concentrations below 0.1 mg m^{-3}. Inside the plumes, vis-

ACPD
10, 22131–22218, 2010

ibility was significantly reduced. The ozone concentration and the humidity inside the plume were often reduced compared to ambient values. Inside the volcanic plumes, a large fraction of volatile particles in the size range below 100 nm was found suggesting that many sulfuric acid droplets formed from the emitted sulfur dioxide. Taking the FSSP results in the limit of non-absorbing particles as reference, the ash particles had effective diameters of up to 5 µm in the fresh plume, decreasing to an order 1 µm in about 3 to 5 days old plumes.

The ash mass concentration depends on the volcano source strength and the plume age besides many other parameters. To first order ash concentration and the SO_2 mixing ratio decreased by a factor of two within less than a day. Estimates of the volume flux and mass fluxes have been provided for the young plume of 1–2 May. The distal ash mass flux was of the order of 1800 kg s^{-1}, estimated from Lidar observations of the plume extent, wind profile, and aerosol backscatter profile, backed by the in-situ observations of the mass concentration in the upper edge of the plume. For SO_2, the mass emission rate was about a factor of 3–4 smaller than for distal ash. The volcano was only moderately active during the 1–2 May period (but stronger than reported at that time). The initial eruption rate was estimated to about 50 times larger than on these two days. Based on these results and the eruption history as given in Fig. 2, the volcano ejected about 40 Tg of ash mass and 10 Tg of SO_2 in total over the April/May period. Certainly, these values are order of magnitude estimates and have to be checked when the eruption flux history is more accurately quantified in other studies. Taking the values for granted, they imply that the Eyjafjalla SO_2 source rate was larger than the values 10 and 140 kg s^{-1} estimated previously for Mt. St. Helens and Mt. Redoubt (Hobbs et al., 1982, 1991). In total, the Eyjafjalla emitted more SO_2 than the recent eruption of Mt. Kasatochi: 1.5 Tg (Karagulian et al., 2010), and less than Mt. Pinatubo in 1991: 20 Tg (McCormick et al., 1995).

The results were used to support aviation agencies in their airspace decisions. From the sum of evidences (visibility, Lidar backscatter, layer depth, particle concentration in the coarse mode, absorption, and later also SO_2 concentration) available during

ACPD
10, 22131–22218, 2010

flight, and comparing to Sahara dust experiences, one could assess early whether the ash loading exceeded 1 mg m^{-3} (1, 2, 16 May) or stayed below 0.2 mg m^{-3} (19, 20, 22 April, 9, 13 May). Besides the measurements, also the fact that the Falcon returned from all the missions without any detectable engine defect from VA supported in assessing aviation safety. In particular, the measurements of 19 April and 9 May over Germany contributed to reopening decisions. The observations of 1–2 May over the North-Atlantic caused an increase of the ash mass source rate used for the VAAC predictions. On the days of 17 and 18 May, a considerable part of air space over Central Europe had more than 0.2 mg m^{-3} but less than 2 mg m^{-3} ash loading. These measurements confirmed VAAC predictions to a degree that closure of air space over Germany could be avoided. The data described in this paper will be used for further studies.

Acknowledgement. The measurements were performed on request of the Deutscher Wetterdienst (DWD, German Weather Service) and the Bundesministerium für Verkehr, Bau und Stadtentwicklung (BMVBS, Federal Ministry of Transport, Building and Urban Development). The flight to Iceland was supported by BMVBS and the Icelandic Air Traffic Control Agency, ISAVIA. We gratefully acknowledge the excellent performance of the pilots Steffen Gemsa, Stefan Grillenbeck, Phillip Weber, Roland Welser, the mechanics Alexander Wolf, the flight dispatchers Andrea Hausold and Frank Probst, the Falcon data processing by Andreas Giez, Volker Dreiling, and Martin Zöger, and the 2D-C probe data analysis by Christophe Gourbeyre. Moreover, we are grateful to support by many further colleagues including Andreas Dörnbrack, Andreas Petzold, Anke Roiger, Martin Wirth, Florian Dahlkötter, Klaus-Dirk Gottschaldt, Thomas Hamburger, Patrick Jöckel, Heinrich Brockstieger, Michael Grossrubatscher, Christian Hinz, Wolfgang Schneider, Robert Uebelacker, Josef Wiesmiller, Stephan Bensberg, Heidi Huntrieser, Sigrun Matthes, Hans Volkert, Andreas Schütz and Johann-Dietrich Wörner of DLR, and Nathalie Benker from TU Darmstadt. Finally, we thank Andreas Petzold for suggestions for improving the paper.

ACPD
10, 22131–22218, 2010

References

Ansmann, A., Tesche, M., Groß, S., et al.: The 16 April 2010 major volcanic ash plume over Central Europe: EARLINET lidar and AERONET photometer observations at Leipzig and Munich, Germany, Geophys. Res. Lett., 37, L13810, doi:10.1029/2010GL043809, 2010.

Arnold, F., Bührke, T., and Qiu, S.: Evidence for stratospheric ozone-depleting heterogeneous chemistry on volcanic aerosols from El Chichón, Nature, 348, 49–50, doi:10.1038/348049a0, 1990.

Balkanski, Y., Schulz, M., Claquin, T., and Guibert, S.: Reevaluation of Mineral aerosol radiative forcings suggests a better agreement with satellite and AERONET data, Atmos. Chem. Phys., 7, 81–95, doi:10.5194/acp-7-81-2007, 2007.

Bandy, A. R., Maroulis, P. J., Wilner, L. A., and Torres, A. L.: Estimates of the fluxes of NO, SO_2, H_2S, CS_2 and OCS from Mt. St. Helens deduced from in situ plume concentration measurements, Geophys. Res. Lett., 9, 1097–1100, doi:10.1029/GL009i009p01097, 1982.

Bonasoni, P., Cristofanelli, P., Calzolari, F., Bonafè, U., Evangelisti, F., Stohl, A., Zauli Sajani, S., van Dingenen, R., Colombo, T., and Balkanski, Y.: Aerosol-ozone correlations during dust transport episodes, Atmos. Chem. Phys., 4, 1201–1215, doi:10.5194/acp-4-1201-2004, 2004.

Borrmann, S., Luo, B., and Mishchenko, M.: Application of the T-matrix method to the measurement of aspherical (ellipsoidal) particles with foreward scattering optical particle counters, J. Aeros. Sci., 31, 789–799, 2000.

Casadevall, T. J.: Volcanic hazards and aviation safety: Lessons of the past decade, Flight Safety Foundation – Flight Safety Digest, May, 1–9, 1993.

Clarke, A. D., Charlson, R. J., and Ogren, J. A.: Stratospheric aerosol light absorption before and after El Chichon, Geophys. Res. Lett., 10, 1017–1020, doi:10.1029/GL010i011p01017, 1983.

Clarke, A. D.: A thermo-optic technique for in situ analysis of size-resolved aerosol physicochemistry, Atmos. Env., A25, 635–644, 1991.

Cronn, D. R. and Nutmagul, W.: Characterization of trace gases in 1980 volcanic plumes of Mt. St. Helens, J. Geophys. Res., 87, 11153–11160, 1982.

Draxler, R. R. and Hess, G. D.: An overview of the HYSPLIT-4 modeling system of trajectories, dispersion, and deposition, Aust. Meteorol. Mag., 47, 295–308, 1998.

Draxler, R. R.: Evaluation of an ensemble dispersion calculation, J. Appl. Meteorol., 42, 308–

ACPD
10, 22131–22218, 2010

317, 2003.
Duce, R. A.: Sources, distributions, and fluxes of mineral aerosols and their relationship to climate, in: Aerosol Forcing of Climate, edited by: Charlson, R. J. and Heintzenberg, J., Wiley, Chichester, 43–72, 1995.
Dunn, M. G. and Wade, D. P.: Influence of Volcanic Ash Clouds on Gas Turbine Engines, Proceedings of the First International Symposium on Volcanic Ash and Aviation Safety, Washington, 1994.
Durant, A. J., Shaw, R. A., Rose, W. I., Mi, Y., and Ernst, G. G. J.: Ice nucleation and overseeding of ice in volcanic clouds, J. Geophys. Res., 113, D09206, doi:10.1029/2007JD009064, 2008.
Ebert, M., Weinbruch, S., Rausch, A., Gorzawski, G., Helas, G., Hoffmann, P., and Wex, H.: Complex refractive index of aerosols during LACE 98 as derived from the analysis of individual particles, J. Geophys. Res., 107, 8121, doi:10.1029/2000JD000195, 2002.
Fiebig, M.: Das troposphärische Aerosol in mittleren Breiten – Mikrophysik, Optik und Klimaantrieb am Beispiel der Feldstudie LACE 98, DLR-Forschungsbericht 2001-23, 259, 2001.
Fiedler, V., Arnold, F., Schlager, H., Dörnbrack, A., Pirjola, L., and Stohl, A.: East Asian SO_2 pollution plume over Europe – Part 2: Evolution and potential impact, Atmos. Chem. Phys., 9, 4729–4745, doi:10.5194/acp-9-4729-2009, 2009.
Flentje, H., Claude, H., Elste, T., Gilge, S., Köhler, U., Plass-Dülmer, C., Steinbrecht, W., Thomas, W., Werner, A., and Fricke, W.: The Eyjafjallajökull eruption in April 2010 – detection of volcanic plume using in-situ measurements, ozone sondes and a new generation ceilometer network, Atmos. Chem. Phys. Discuss., 10, 14947–14968, doi:10.5194/acpd-10-14947-2010, 2010.
Gayet, J.-F., Shcherbakov, V., Mannstein, H., Minikin, A., Schumann, U., Ström, J., Petzold, A., Ovarlez, J., and Immler, F.: Microphysical and optical properties of midlatitude cirrus clouds observed in the Southern Hemisphere during INCA, Q. J. Roy. Meteorol. Soc., 132, 2719–2748, doi: 10.1256/qj.05.162, 2006.
Gayet, J.-F., Treffeisen, R., Helbig, A., Bareiss, J., Matsuki, A., Herber, A., and Schwarzenboeck, A.: On the onset of the ice phase in boundary layer Arctic clouds, J. Geophys. Res., 114, D19201, doi:10.1029/2008JD011348, 2009.
Gerbig, C., S. Schmitgen, D. Kley, Volz-Thomas, A., Dewey, K., and Haaks, D.: An improved fast-response vacuum-UV resonance fluorescence CO instrument, J. Geophys. Res., 104,

ACPD
10, 22131–22218, 2010

1699–1704, 1999.
Grindle, T. J. and Burcham Jr., F. W.: Even minor volanic ash encounters can cause major damage to aircraft, ICAO Journal, November, 7–10, 2002.
Grindle, T. J. and Burcham Jr., F. W.: Engine Damage to a NASA DC-8-72 Airplane From a High-Altitude Encounter With a Diffuse Volcanic Ash Cloud, National Aeronautics and Space Administration, Dryden Flight Research Center, Edwards, California 93523-0273, NASA/TM-2003-212030, 2003.
Hansen, J. E. and Travis, L. D.: Light scattering in planetary atmospheres, Space Sci. Rev., 16, 527–610, 1974.
Heue, K.-P., Brenninkmeijer, C. A. M., Wagner, T., Mies, K., Dix, B., Frieß, U., Martinsson, B. G., Slemr, F., and van Velthoven, P. F. J.: Observations of the 2008 Kasatochi volcanic SO_2 plume by CARIBIC aircraft DOAS and the GOME-2 satellite, Atmos. Chem. Phys., 10, 4699–4713, doi:10.5194/acp-10-4699-2010, 2010.
Hinds, W. C.: Aerosol Technology, John Wiley & Sons, New York, 504 pp., 1999.
Hobbs, P., Tuell, J., Hegg, D., Radke, L., and Eltgroth, M.: Particles and gases in the emissions from the 1980–1981 volcanic eruptions of Mt. St. Helens, J. Geophys. Res., 87, 11062–11086, 1982.
Hobbs, V. P., Radke, L. F., Lyons, J. H., Ferek, R. J., Coffman, D. J., and Casadevall, T. J.: Airborne measurements of particle and gas emissions from the 1990 volcanic eruptions of Mount Redoubt, J. Geophys. Res., 96, 18735–18752, 1991.
Hunton, D. E., Viggiano, A. A., Miller, T. M., et al.: In-situ aircraft observations of the 2000 Mt. Hekla volcanic cloud: Composition and chemical evolution in the Arctic lower stratosphere, J. Volcanol. Geoth. Res., 145, 23–34, 2005.
ICAO: Volcanic Ash Contingency Plan – EUR and NAT regions, International Civil Aviation Authority, Montreal, 1–25, 2010.
Jones, A., Johnson, D., Hort, M., and Devenish, B.: The UK Met Office's Next-Generation Atmospheric Dispersion Model, NAME III, in: Air Pollution Modeling and Its Application XVII, edited by: Borrego, C., and Norman, A.-L., Springer, doi:10.1007/978-0-387-68854-1, 580–589, 2007.
Jurkat, T., Voigt, C., Arnold, F., Schlager, H., Aufmhoff, H., Schmale, J., Schneider, J., Lichtenstern, M., and Dörnbrack, A.: Airborne stratospheric ITCIMS-measurements of SO_2, HCl, and HNO_3 in the aged plume of volcano Kasatochi, J. Geophys. Res., in press, doi:10.1029/2010JD013890, 2010.

ACPD
10, 22131–22218, 2010

Kandler, K., Schütz, L., Deutscher, C., et al.: Size distribution, mass concentration, chemical and mineralogical composition and derived optical parameters of the boundary layer aerosol at Tinfou, Morocco, during SAMUM, Tellus, 61B, 32–50, doi:10.1111/j.1600-0889.2008.00385.x, 2009.

Kandler, K., von Glahn, C., Lieke, K., Wilhelm, K.-D., Ebert, M., Nillius, B., Petzold, A., Schütz, L., Weinzierl, B., and Weinbruch, S.: A giant particle collector (GPaC) for collection of super micron particles on an aircraft platform, International Aerosol Conference, Abstr. 145, Helsinki, Finland, 2010.

Karagulian, F., Clarisse, L., Clerbaux, C., Prata, A. J., Hurtmans, D., and Coheur, P. F.: Detection of volcanic SO_2, ash, and H_2SO_4 using the Infrared Atmospheric Sounding Interferometer (IASI), J. Geophys. Res., 115, D00L02, doi:10.1029/2009JD012786, 2010.

Köpp, F., Rahm, S., and Smalikho, I.: Characterization of aircraft wake vortices by 2-µm pulsed Doppler lidar, J. Atmos. Ocean. Tech., 21, 194–206, 2004.

Kotra, J. P., Finnigan, D. L., Zoller, W. H., Hart, M. A., and Moyers, J. L.: El Chichón: Composition of plume gases and particles, Science, 222, 1018–1021, doi:10.1126/science.222.4627.1018, 1983.

Krotkov, N. A., Flittner, D. E., Krueger, A. J., Kostinski, A., Riley, C., Rose, W., and Torres, O.: Effect of particle non-sphericity on satellite monitoring of drifting volcanic ash clouds, J. Quant. Spectrosc. Ra., 63, 613–630, 1999.

Lawson, R. P., O'Connor, D., Zmarzly, P., Weaver, K., Baker, B., Mo, Q., and Jonsson, H.: The 2D-S (stereo) probe: Design and preliminary tests of a new airborne, high-speed, high-resolution particle imaging probe, J. Atmos. Ocean. Tech., 23, 1462–1477, 2006.

Lilly, D. K.: Cirrus outflow dynamics, J. Atmos. Sci., 45, 1594–1605, 1988.

Luke, W. T.: Evaluation of a commercial pulsed flurescence detector for the measurements of low-level SO_2 concentrations during the Gas-Phase Sulfur Intercomparison Experiment, J. Geophys. Res., 102, 16255–16265, 1997.

Martinsson, B. G., Brenninkmeijer, C. A. M., Carn, S. A., Hermann, M., Heue, K.-P., van Velthoven, P. F. J., and Zahn, A.: Influence of the 2008 Kasatochi volcanic eruption on sulfurous and carbonaceous aerosol constituents in the lower stratosphere, Geophys. Res. Lett., 36, L12813, doi:10.1029/2009GL038735, 2009.

Mason, B. G., Pyle, D. M., and Oppenheimer, C.: The size and frequency of the largest explosive eruptions on Earth, Bull. Volcanol., 66, 735–748, DOI 10.1007/s00445-004-0355-9, 2004.

ACPD
10, 22131–22218, 2010

Mastin, L. G., Guffanti, M., Servranckx, R., et al.: A multidisciplinary effort to assign realistic source parameters to models of volcanic ash-cloud transport and dispersion during eruptions, J. Volcanol. Geoth. Res., 186, 10–21, 2009.
McCormick, M. P., Thomason, L. W., and Trepte, C. R.: Atmospheric effects of the Mt Pinatubo eruption, Nature 373, 399–404, doi:10.1038/373399a0, 1995.
McFarquhar, G. M. and Heymsfield, A. J.: The definition and significance of an effective radius for ice clouds, J. Atmos. Sci., 55, 2039–2052, 1998.
Minikin, A., Petzold, A., Ström, J., Krejci, R., Seifert, M., van Velthoven, P., Schlager, H., and Schumann, U.: Aircraft observations of the upper tropospheric fine particle aerosol in the Northern and Southern Hemispheres at midlatitudes, Geophys. Res. Lett., 30, 1503, doi:10.1029/2002gl016458, 2003.
Mishchenko, M. I. and Travis, L. D.: Light scattering by polydispersions of randomly oriented spheroids with sizes comparable to wavelenghts of observation, Appl. Opt., 33, 7206–7225, 1994.
Mishchenko, M. I. and Travis, L. D.: Capabilities and limitations of a current FORTRAN implementation of the T-matrix method for randomly oriented, rotationally symmetric scatterers, J. Quant. Spectrosc. Ra., 60, 309–324, doi:10.1016/S0022-4073(98)00008-9, 1998.
Munoz, O., Volten, H., Hovenier, J. W., Veihelmann, B., v. d. Zande, W. J., Waters, L. B. F. M., and Rose, W. I.: Scattering matrices of volcanic ash particles of Mount St. Helens, Redoubt, and Mount Spurr Volcanoes, J. Geophys. Res., 109, D16201, doi:10.1029/2004JD004684, 2004.
Ouimette, J. R. and Flagan, R. C.: The extinction coefficient of multicomponent aerosols, Atmos. Env., 16, 2405–2419, 1982.
Patterson, E. M.: Optical properties of the crustal aerosol: Relation to chemical and physical characteristics, J. Geophys. Res., 86, 3236–3246, doi:10.1029/JC086iC04p03236, 1981.
Patterson, E. M., Pollard, C. O., and Galindo, I.: Optical properties of the ash from El Chichon Volcano, Geophys. Res. Lett., 10, 317–320, doi:10.1029/GL010i004p00317, 1983.
Petzold, A., Rasp, K., Weinzierl, B., et al.: Saharan dust absorption and refractive index from aircraft-based observations during SAMUM 2006, Tellus, 61B, 118–130, doi:10.1111/j.1600-0889.2008.00383.x, 2009.
Pieri, D., Ma, C., Simpson, J. J., Hufford, G., Grindle, T., and Grove, C.: Analyses of in-situ airborne volcanic ash from the February 2000 eruption of Hekla Volcano, Iceland, Geophys. Res. Lett., 29, 1767, 10.1029/2001GL013688, 2002.

ACPD
10, 22131–22218, 2010

Pollack, J. B., Toon, O. B., and Khare, B. N.: Optical properties of some terrestrial rocks and glasses, Icarus, 19, 372–389, 1973.
Prata, A. J. and Grant, I. F.: Retrieval of microphysical and morphological properties of volcanic ash plumes from satellite data: Application to Mt. Ruapehu, New Zealand, Q. J. Roy. Meteorol. Soc., 127, 2153–2179, 2001.
Prata, A. J.: Satellite detection of hazardous volcanic clouds and the risk to global air traffic, Natural Hazards, 51, 303–324, doi:10.1007/s11069-008-9273-z, 2009.
Przedpelski, Z. J., and Casadevall, T. J.: Impact of volcanic ash from 15 December 1989 Redoubt volcano eruption on GE CF6-80C2 turbofan engines, Proceedings of the First International Symposium on Volcanic Ash and Aviation Safety, Washington, 1994.
Reitebuch, O., Werner, C., Leike, I., Delville, P., Flamant, P. H., Cress, A., and Engelbart, D.: Experimental validation of wind profiling performed by the airborne 10-µm-heterodyne Doppler lidar WIND, J. Atmos. Ocean. Tech., 18, 1331–1344, 2001.
Reitebuch, O., Lemmerz, C., Nagel, E., Paffrath, U., Durand, Y., Endemann, M., Fabre, F., and Chaloupy, M.: The Airborne Demonstrator for the Direct-Detection Doppler Wind Lidar ALADIN on ADM-Aeolus: I. Instrument design and comparison to satellite instrument, J. Atmos. Ocean. Tech., 26, 2501–2515, doi 10.1175/2009JTECHA1309.1, 2009.
Roiger, A.: Shipboard sulfur dioxide measurements in the North Atlantic marine boundary layer, Master thesis, Munich University of Applied Sciences, 2007.
Rose, W. I., Millard, G. A., Mather, T. A., et al.: Atmospheric chemistry of a 33–34 hour old volcanic cloud from Hekla Volcano (Iceland): Insights from direct sampling and the application of chemical box modeling, J. Geophys. Res., 111, D20206, doi:10.1029/2005JD006872, 2006.
Rose, W. I. and Durant, A. J.: Fine ash content of explosive eruptions, J. Volcanol. Geoth. Res., 186, 32–39, doi:10.1016/j.jvolgeores.2009.01.010, 2009.
Schlager, H., Konopka, P., Schulte, P., Schumann, U., Ziereis, H., Arnold, F., Klemm, M., Hagen, D. E., Whitefield, P. D., and Ovarlez, J.: In situ observations of air traffic emission signatures in the North Atlantic flight corridor, J. Geophys. Res., 102, 10739–10750, 1997.
Schmale, J., Schneider, J., Jurkat, T., et al.: Aerosol layers from the 2008 eruptions of Mount Okmok and Mount Kasatochi: In situ upper troposphere and lower stratosphere measurements of sulfate and organics over Europe, J. Geophys. Res., 115, D00L07, doi:10.1029/2009JD013628, 2010.
Schröder, F. and Ström, J.: Aircraft measurements of sub micrometer aerosol particles (>7 nm)

ACPD
10, 22131–22218, 2010

in the midlatitude free troposphere and tropopause region, Atmos. Res., 44, 333–356, 1997.
Schumann, U., Arnold, F., Busen, R., Curtius, J., Kärcher, B., Curtius, J., Petzold, A., Schlager, H., Schröder, F., and Wohlfrom, K. H.: Influence of fuel sulfur on the composition of aircraft exhaust plumes: The experiments SULFUR 1–7, J. Geophys. Res., 107, 4247, doi:10.1029/2001JD000813, 2002.
Schumann, U., Mayer, B., Gierens, K., Unterstrasser, S., Jessberger, P., Petzold, A., and Voigt, C.: Effective radius of ice particles in cirrus and contrails, J. Atmos. Sci., doi:10.1175/2010JAS3562.1, in press, 2010.
Schütz, L.: Long range transport of desert dust with special emphasis on the Sahara, Ann. N.Y. Acad. Sci., 338, 515–532, doi:10.1111/j.1749-6632.1980.tb17144.x, 1980.
Seibert, P. and Frank, A.: Source-receptor matrix calculation with a Lagrangian particle dispersion model in backward mode, Atmos. Chem. Phys., 4, 51–63, doi:10.5194/acp-4-51-2004, 2004.
Sokolik, I. N. and Toon, O. B.: Incorporation of mineralogical composition into models of the radiative properties of mineral aerosol from UV to IR wavelengths, J. Geophys. Res., 104, 9423–9444, doi:10.1029/1998JD200048, 1999.
Sparks, R. S. J., Bursik, M. I., Carey, S. N., Gilbert, J. S., Graze, L. S., Sigurdsson, H., and Woods, A. W.: Volcanic Plumes, J. Wiley and Sons, Chichester, 574 pp., 1997.
Stohl, A., Forster, C., Eckhardt, S., Spichtinger, N., Huntrieser, H., Heland, J., Schlager, H., Wilhelm, S., Arnold, F., and Cooper, O.: A backward modeling study of intercontinental pollution transport using aircraft measurements, J. Geophys. Res., 108, 4370, doi:10.1029/2002JD002862, 2003.
Stohl, A., Forster, C., Frank, A., Seibert, P., and Wotawa, G.: Technical note: The Lagrangian particle dispersion model FLEXPART version 6.2, Atmos. Chem. Phys., 5, 2461–2474, doi:10.5194/acp-5-2461-2005, 2005.
Strapp, J. W., Leaitch, W. R., and Liu, P. S. K.: Hydrated and dried aerosol-size-distribution measurements from the particle measuring systems FSSP-300 probe and the deiced PCASP-100X probe, J. Atmos. Ocean. Techn., 9, 548–555, 1992.
Tröger, W. E.: Optische Bestimmung der gesteinsbildenden Minerale Teil I.: Bestimmungstabellen, edited by: Bambauer, H. U., Taborszky, F. and Trochim, H.-D., Schweitzerbartsche Verlagsbuchhandlung, Stuttgart, 1982.
Virkkula, A.: Correction of the calibration of the 3-wavelength Particle Soot Absorption Photometer (3λ PSAP), Aerosol Sci. Techn., 44, 706–712, 2010.

ACPD
10, 22131–22218, 2010

Voigt, C., Schumann, U., Jurkat, T., Schäuble, D., Schlager, H., Petzold, A., Gayet, J.-F., Krämer, M., Schneider, J., Borrmann, S., Schmale, J., Jessberger, P., Hamburger, T., Lichtenstern, M., Scheibe, M., Gourbeyre, C., Meyer, J., Kübbeler, M., Frey, W., Eichler, H., Butler, T., Lawrence, M. G., Holzäpfel, F., Arnold, F., Wendisch, M., Döpelheuer, A., Gottschaldt, K., Baumann, R., Zöger, M., Sölch, I., Rautenhaus, M., and Dörnbrack, A.: In-situ observations of young contrails – overview and selected results from the CONCERT campaign, Atmos. Chem. Phys. Discuss., 10, 12713–12763, doi:10.5194/acpd-10-12713-2010, 2010.

von Glasow, R.: Atmospheric chemistry in volcanic plumes, P. Natl. Acad. Sci. USA, 107, 6594–6599, 2010.

Watson, I. M. and Oppenheimer, C.: Photometric observations of Mt. Etna's different aerosol plumes, Atmos. Env., 35, 3561–3572, 2001.

Webley, P. and Mastin, L.: Improved prediction and tracking of volcanic ash clouds, J. Volcanol. Geoth. Res., 186, 1–9, 2009.

Weinzierl, B., Petzold, A., M.Esselborn, Wirth, M., Rasp, K., Kandler, L., Schütz, L., Koepke, P., and Fiebig, M.: Airborne measurements of dust layer properties, particle size distribution and mixing state of Saharan dust during SAMUM 2006, Tellus, 61B, 96–117, doi:10.1111/j.1600-0889.2008.00392.x, 2009.

Weissmann, M., Braun, F. J., Gantner, L., Mayr, G., Rahm, S., and Reitebuch, O.: The Alpine mountain-plain circulation: Airborne Doppler lidar measurements and numerical simulations, Mon. Wea. Rev., 133, 3095–3109, 2005a.

Weissmann, M., Busen, R., Dörnbrack, A., Rahm, S., and Reitebuch, O.: Targeted observations with an airborne wind lidar, J. Atmos. Ocean. Techn., 22, 1706–1719, 2005b.

Wendisch, M., Coe, H., Baumgardner, D., et al.: Supplement to aircraft particle inlets: State-of-the-art and future needs, B. Am. Meteorol. Soc., 85, 92–92, 2004.

Winker, D. M. and Osborn, M. T.: Airborne lidar observations of the Pinatubo volcanic plume, Geophys. Res. Lett., 19, 167–170, doi:10.1029/91GL02867, 1992.

ACPD
10, 22131–22218, 2010

Table 1. Falcon instrumentation for the DLR volcanic ash missions in April/May 2010.

Instrumentation	Measured quantity
Remote sensing instrument	
2-µm Wind-Lidar	Vertical profile of attenuated aerosol backscatter and wind vector below the aircraft
Aerosol in-situ instruments	
Multi-channel condensation particle counter (CPC; 3 unheated, 2 heated channels)	Integral number of ultrafine particles ($0.005<D<2.5\,\mu m$) and non-volatile fraction
2-channel Optical Particle Counter (Grimm OPC 1.129)	Total and non-volatile size distribution ($0.25\,\mu m<D<2.5\,\mu m$)
Three-wavelength Particle Soot Absorption Photometer (3-λ-PSAP)	Absorption coefficient at λ=467, λ=530 and λ=660 nm
Passive Cavity Aerosol Spectrometer Probe (PCASP-100X)	Size distribution accumulation mode, dry state ($0.15\,\mu m<D<3.0\,\mu m$)
Forward Scattering Spectrometer Probe (FSSP-300)	Size distribution coarse mode, ambient state ($1\,\mu m<D<30\,\mu m$)
Two-dimensional imaging cloud probe (2D-C)	Shape and size distribution of very large particles, water droplets and ice-crystals ($25\,\mu m<D<800\,\mu m$)
Impactor sampler	Chemical composition and shape of sub-2.5 µm particles
Giant Particle Collector (GPaC)	Chemical composition in the coarse mode
Trace gas in-situ instruments	
SO_2 detector (fluorescence)	Sulfur dioxide mixing ratio
O_3 detector (UV absorption)	Ozone mixing ratio
CO detector (vacuum UV)	Carbon monoxide mixing ratio
Meteorological data	
Falcon standard instrumentation	Position, temperature, pressure, humidity, wind
CR-2 dew point hygrometer	Dew point, humidity

ACPD
10, 22131–22218, 2010

Table 2. List of Falcon flights during the DLR volcanic ash missions in April/May 2010.

Date	Take-off time (UTC)	Landing time (UTC)	Mission objective
19 Apr	14:12:02	17:54:50	Aged ash plume over Germany and The Netherlands (air space in Europe largely closed)
22 Apr	14:14:14	15:35:09	Lidar survey over Germany
22 Apr	17:12:55	20:29:30	Aged ash plume south of Norway (embedded in clouds)
23 Apr	11:45:56	14:57:46	Aged ash plume over Germany, Poland and Baltic Sea
29 Apr	12:00:10	14:09:06	Ferry flight to Edinburgh
29 Apr	15:39:59	18:28:50	Flight to Iceland with Lidar survey of ash plume and in-situ profiling at Keflavik airport
1 May	10:50:29	14:05:03	Lidar survey of fresh ash plume near volcano and in-situ profiling at Keflavik airport
2 May	12:58:36	16:17:57	Flight from Keflavik to Stornoway with in-situ measurement in the top part of the fresh plume over the North Atlantic
3 May	11:04:40	13:31:27	Ferry flight to Oberpfaffenhofen
9 May	14:26:52	18:01:24	Aged ash plume over Germany (Munich and Stuttgart airports and air space closed for 6 h)
13 May	10:06:25	11:20:04	Ferry flight to Niederrhein (Germany)
	12:44:26	15:49:47	Aged ash plume in the Southwest North Sea
16 May	09:11:17	11:07:31	Ferry flight to Newquay (UK)
16 May	12:34:50	16:01:16	Aged ash plume over Irish Sea and Northern England (UK air space partly closed)
17 May	10:38:47	13:29:50	Aged ash plumes over Germany, The Netherlands and the North Sea
17 May	14:36:54	17:57:00	Aged dense ash plume over North Sea, extensive in-situ measurement
18 May	07:25:32	10:34:56	Aged ash plume survey over Germany and North Sea (German air space closure was under consideration)

ACPD
10, 22131–22218, 2010

Table 3. Plume properties at selected flight legs.

Leg		1	2	3	4	5	6	7	8	9	10	11	12
Position	Unit	Leipzig	Stuttgart	Munich/Maisach	Skagerrak	Baltic Sea	North Atlantic	Munich/Maisach	SW North Sea	NE England	North Sea	Hamburg	Stuttgart
Date	d.mon	19.04	19.04	19.04	22.04	23.04	02.05	09.05	13.05	16.05	17.05	18.05	18.05
Leg start time	h:min:s	15:08:35	17:18:55	17:40:15	19:10:35	12:36:57	15:11:25	14:56:15	14:11:35	14:08:35	15:50:45	09:22:35	10:13:15
Leg end time	h:min:s	15:15:35	17:21:25	17:43:45	19:12:55	12:37:59	15:14:35	15:00:35	14:15:15	14:15:55	16:57:35	09:30:45	10:16:45
Longitude	°E	12.45	9.63	11.09	8.57	16.52	−15.17	12.6	1.45	−0.17	2.92	9.12	9.97
Latitude	°N	51.29	48.58	47.89	58.05	54.66	60.17	48.38	53.41	54.76	52.83	53.17	48.87
Height	km	4.2±0.2	3.8±0.1	4.0±0.1	2.6±0.0	2.7±0.0	3.5±0.2	4.1±0.2	5.1±0.0	6.1±0.4	5.2±1.6	3.1±0.1	5.2±0.1
Pressure	hPa	598	634.5	621	725.4	724.4	661.5	609.4	528.6	459.9	530.7	697.3	527.9
Temperature	°C	−14.4	−9.8	−10.8	−13.2	−12.8	−6.3	−11.8	−22.0	−28.5	−23.7	−7.3	−21.3
Wind speed	$m\,s^{-1}$	15.8	7.4	6.7	6.4	15.8	15.4	9.1	12.9	10.2	13.9	7.5	16.2
Wind direction	°	270	293	318	288	267	330	250	196	225	340	304	304
SO_2 mixing ratio	10^{-9}	–	–	–	1.8	0.6	74.9	3.6	9.7	14.3	27	14.3	4.6
CO mixing ratio	10^{-9}	129.5	135.7	138.5	140.5	138.4	200.9	130.6	121.8	116.6	133.9	125.4	117.2
CO background	10^{-9}	129.0	135.0	138	140.5	138.5	128.5	129.0	114.0	108.0	120.0	115.0	115.0
O_3 mixing ratio	10^{-9}	55.6	53.6	57.3	46.6	55.9	30.1	54.2	51.9	114.3	59.5	85.5	74.4
O_3 background	10^{-9}	55.0	53.5	57.0	57.0	53.0	52.0	59.0	59.0	130.0		110.0	110.0
Rel. humidity liq.	%	17	17.7	13.7	56.1	66.5	59.2	74.6	49.2	8.3	32	17	11.2
Aitken particles	cm^{-3}	756	818	585	5451	7436	6848	2055	5176	5525	4903	2165	1610
Aitken non vol.	cm^{-3}	187	196	227	200	351	3334	677	189	154	215	278	219
Accumulation	cm^{-3}	11.9	10.4	9.9	3	6.7	28.4	23.9	4	12.6	20.6	19.7	6.7
Accum. non vol.	cm^{-3}	5.6	5.2	4.3	0.9	0.9	21.2	0.9	1.4	5.6	11.4	7	2.3
Coarse mode	cm^{-3}	0.30	0.25	0.20	0.02	0.03	0.88	0.04	0.06	0.13	0.78	0.30	0.13
Super coarse	cm^{-3}	0.0073	0.0048	0.0052	0.0053	0.0050	0.0793	0.0008	0.0013	0.0024	0.0681	0.0173	0.0056
Mass conc. (N)	$\mu g\,m^{-3}$	29	22	17	22	5	206	8	9	15	180	55	24
Mass conc. (A)	$\mu g\,m^{-3}$	110	91	46	160	7	869	18	42	53	742	219	104
Max. MC (N)	$\mu g\,m^{-3}$	78	63	41	–	5	553	27	31	48	462	145	43
Max MC (A)	$\mu g\,m^{-3}$	475	416	177	–	9	2619	123	271	330	2371	781	211
D_{eff} (N)	µm	3.1	3.3	2.4	3.1	1.0	3.7	0.4	1.6	1.9	4.7	2.7	3.2
D_{eff} (A)	µm	7.5	8.8	4.8	7.2	1.4	10.3	0.8	4.7	4.7	12.1	7.7	9.4
Age FLEXPART	h	111	108	108	50	58	12	129	78	66	66–82	81	66
Age HYSPLIT	h	105	104	105	49	40	7.1	97	71	58	76–88	100	78
Source altitude	km	4.5–5.7	3.5–6	4.6–5.5	na	2.8–3.2	2.6–2.9	3–6	2–7	1.8–3	1.8–3	2.5–4.5	3–8
Source strength	rel. units	5–20	3–15	3–15	0.2–1.5	0.2–3	0.5–2	2–10	1–6	5–20	3–50	3–15	3–15
Layer top	km	5.6*	3.8	4.2	5.5**	3.4*	3.7*	4.9	5.4***	7.0*	6.3*	3.4	5.7*
Layer bottom	Km	3.9*	3.5	3.9	0.7**	2.1*	1.6*	3.5	2.8***	3.6*	3.2*	2.8	4.0*

Explanations. Height: flight altitude from Global Positioning System data, GPS. Aitken-Mode: 10–160 nm. Accumulation mode: from instrument Grimm OPC 1.129, 0.25–1.0 µm. Coarse mode: from FSSP-300 channels 13–29, 2–50 µm for analysis A, absorbing refractive index value, m=1.59+0.004i, and 2–25 µm for analysis N, non-absorbing index m=1.59+0.0i. Super coarse mode: from FSSP-300 channels 18–29, 6.5–50 µm for A, 5–25 µm for N. Mass conc.: mass concentration for non-absorbing (N) and absorbing (A) refractive index values. Max MC: Maximum of 10-s mean values of mass concentration for material N and A. D_{eff}=3×specific volume/(2×specific cross-section area)=effective diameter, for non-absorbing (N) and absorbing refractive index (A). Age= plume age from backward trajectories (resolution of FLEXPART: 0.5°×0.5°, HYSPLIT: 1°×1°). Altitude=altitude of backward trajectory above the volcano. Source=source strength of volcano at the time when the trajectory started from the volcano (from Fig. 2). Layer depth=geometrical depth of the ash layer as derived from the Lidar observations (layer top/bottom values with *: include multiple layers; **: no clear layer identified; ***: tilted layer of depth 400–700 m).

ACPD
10, 22131–22218, 2010

Table 4. Number of investigated particles, measured two-dimensional aspect ratio and calculated density and complex refractive index values m for different particle size classes and wavelengths.

	2 May 2010				17 May 2010			
Size/µm	<0.5	0.5–1	1–2	>2	< 0.5	0.5–1	1–2	>2
Number	194	101	136	87	166	167	149	7
Aspect ratio	1.9	2.2	2	2.1	1.8	2.1	2.1	2.0
density	1.8	2.6	2.7	2.7	1.7	2.8	2.7	2.7
m (630 nm)	1.53+ 0.001i	1.60+ 0.004i	1.58+ 0.002i	1.56+ 0.001i	1.55+ 0.001i	1.59+ 0.003i	1.57+ 0.001i	–
m (2 µm)	1.50+ $2\times10^{-6}i$	1.56+ $40\times10^{-6}i$	1.55+ $20\times10^{-6}i$	1.54+ $10\times10^{-6}i$	1.53+ $7\times10^{-6}i$	1.56+ $20\times10^{-6}i$	1.55+ $10\times10^{-6}i$	–

ACPD
10, 22131–22218, 2010

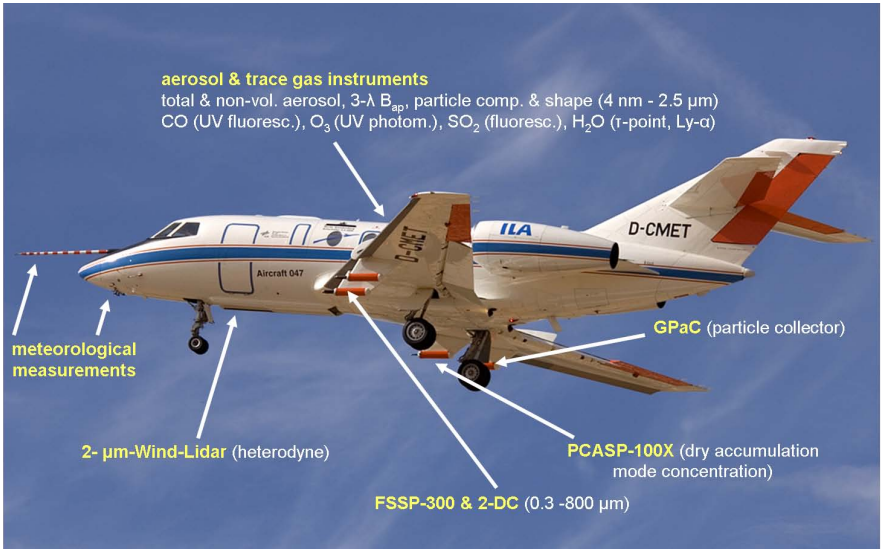

Fig. 1. DLR-research aircraft Falcon and its instrumentation during the volcanic ash flights.

ACPD
10, 22131–22218, 2010

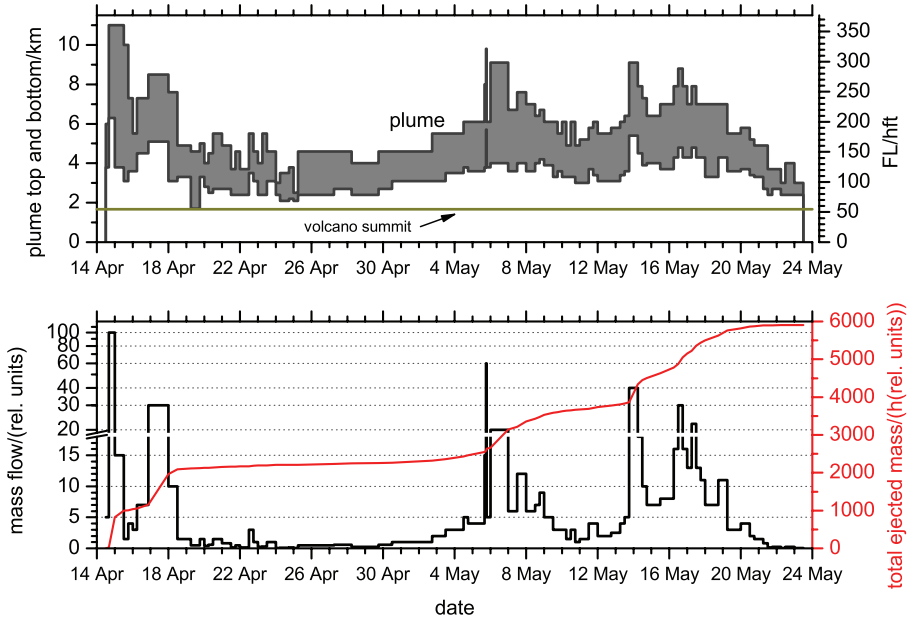

Fig. 2. Ash source characteristics used in the model. The upper panel depicts the ejection height (upper and lower bound, shaded area; FL=flight level in hectofeet). The lower panel shows the mass flow rate and the cumulative mass (red line) in relative (rel.) units. The unit mass flow rate corresponds to a plume top at 4572 m (FL 150).

ACPD
10, 22131–22218, 2010

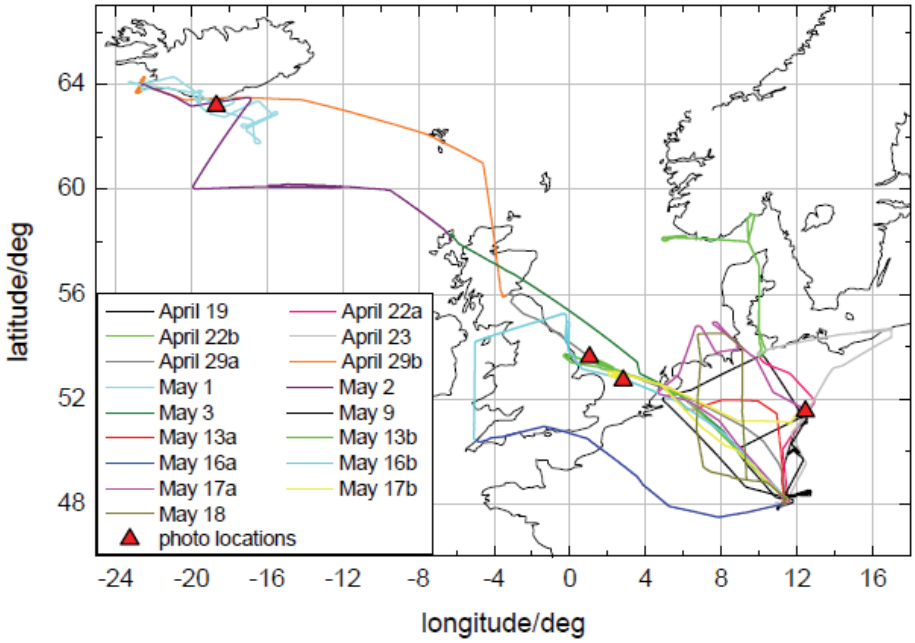

Fig. 3. Flight routes of DLR Falcon during the volcanic ash mission in April/May 2010. The photos shown in Fig. 11 were taken at the positions identified by triangles.

ACPD
10, 22131–22218, 2010

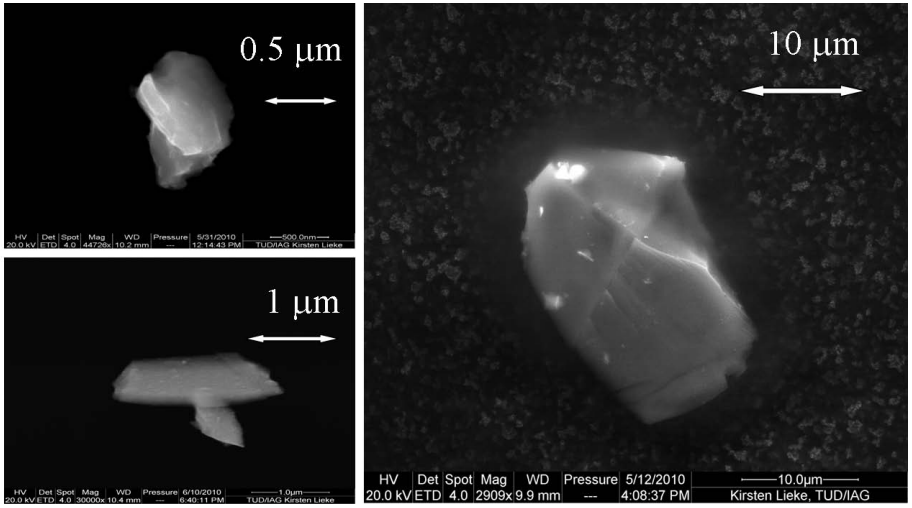

Fig. 4. Typical volcanic ash particles from the plume penetration over the North Atlantic on 2 May 2010. Left: sampled inside the fuselage, right: sampled outside. Particle sizes 0.7, 2, and 20 µm.

ACPD
10, 22131–22218, 2010

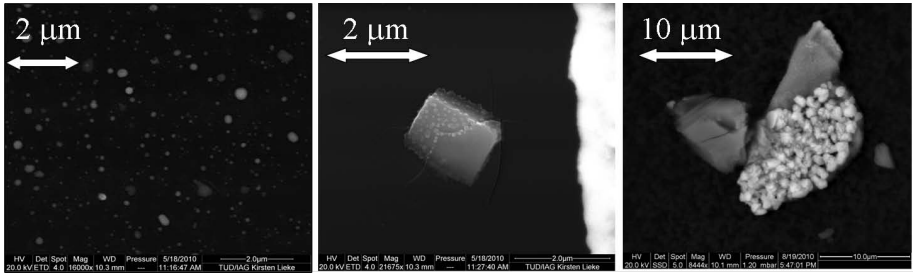

Fig. 5. Examples of ammonium sulfate particles (left), an ammonium sulfate particle with droplets of sulfuric acid (middle) and an agglomerate of large and small particles (right) from the sample of 2 May.

ACPD
10, 22131–22218, 2010

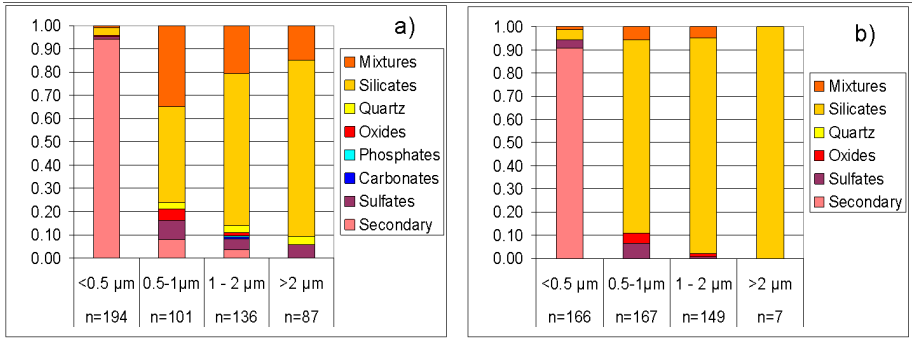

Fig. 6. Relative number abundance of particles with different chemical composition in different size bins for two sampling days (**a**: 15:01–15:15 UTC 2 May, **b**: 16:20–16:24 UTC 17 May). Here, *n* is the total number of particles analyzed in each size bin.

ACPD
10, 22131–22218, 2010

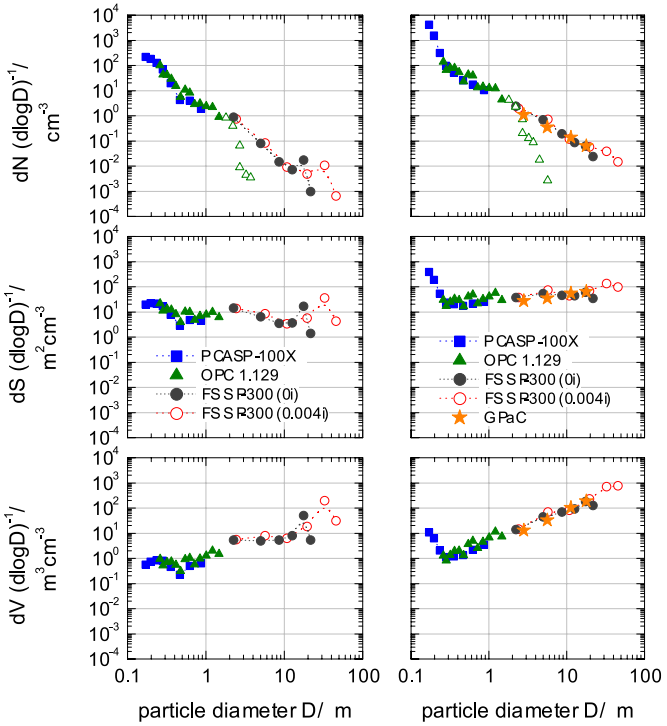

Fig. 7. Particle number N, surface S, and volume V per unit size interval and unit ambient volume versus particle diameter D averaged over the flight legs 1 and 6 of Table 3, i.e. Leipzig, 19 April (left panels), and North Atlantic, 2 May 2010 (right panels). PCASP-100X data points are given as blue square symbols, SKY-OPC data as black triangles (open symbols represent particle sizes affected by low penetration efficiency of the inlet). Circles of different colors represent FSSP-300 data of different refractive index values; red for particles with absorbing component (case A, m=1.59+0.004i), and black for particles without absorption (case N, m=1.59+0i). The stars (right panels only) indicate the scaled size distribution of particles collected by the GPaC impactors on 2 May; the scaling in the concentration axis is fitted to the FSSP results.

ACPD
10, 22131–22218, 2010

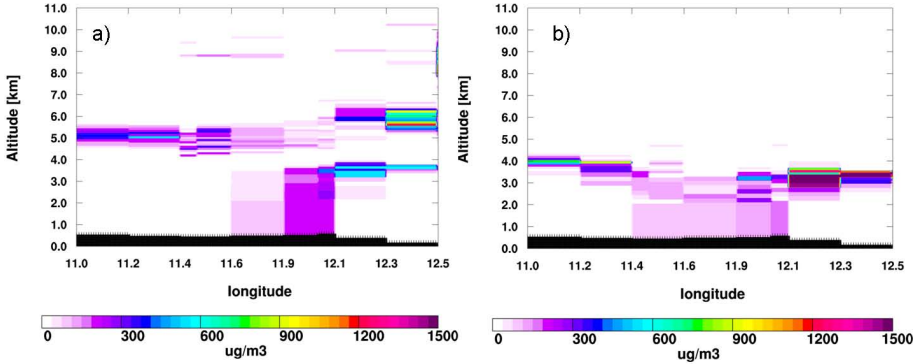

Fig. 8. Vertical cross section along Falcon flight path from Oberpfaffenhofen (48.1° N, 11.2° E) to Leipzig (51.4° N, 12.4° E) for 15:00 UTC 19 April 2010, as computed with FLEXPART. **(a)** Aerosol simulated without sedimentation and deposition (maximum concentration 1328 µg m^{-3}), **(b)** 5-µm aerosol simulated including wet and dry deposition and sedimentation (max. concentration: 2208 µg m^{-3}).

ACPD
10, 22131–22218, 2010

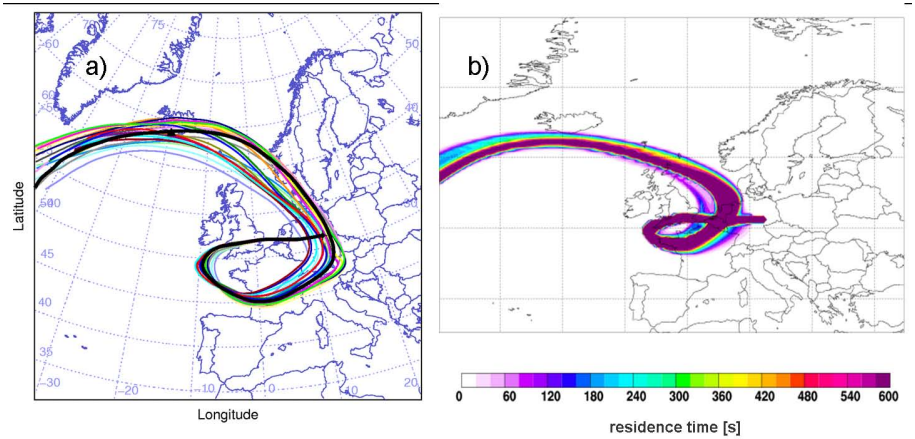

Fig. 9. Backward trajectories starting at 4.2 km altitude near Leipzig at 15:10 UTC 19 April (Table 3, leg 1). **(a)** The curves represent an ensemble of 27 backward trajectories, computed with HYSPLIT. **(b)** Ash mass residence times for the backward trajectories computed with FLEXPART.

ACPD
10, 22131–22218, 2010

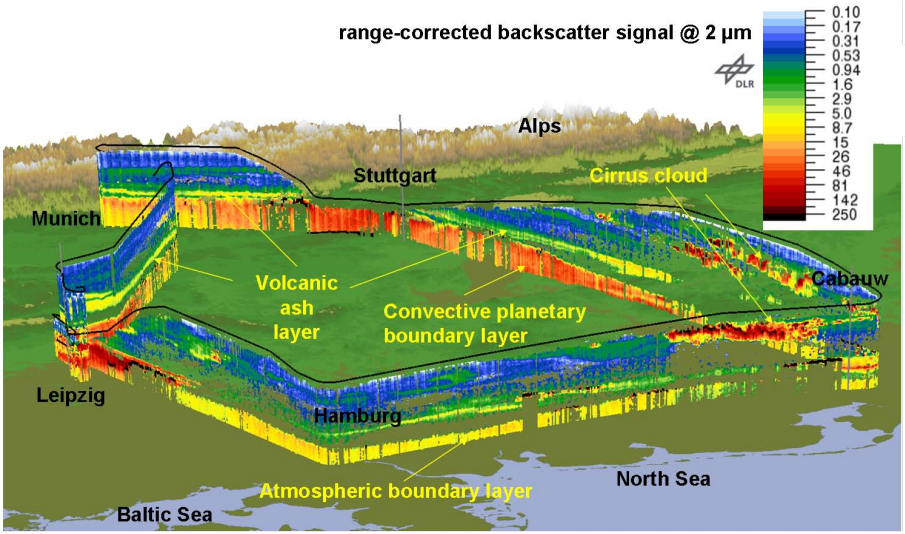

Fig. 10. Lidar cross-section (range corrected backscatter) along flight path over Germany and the Netherlands, 19 April 2010; with various aerosol layers and cities identified. Viewing direction from North to South.

ACPD
10, 22131–22218, 2010

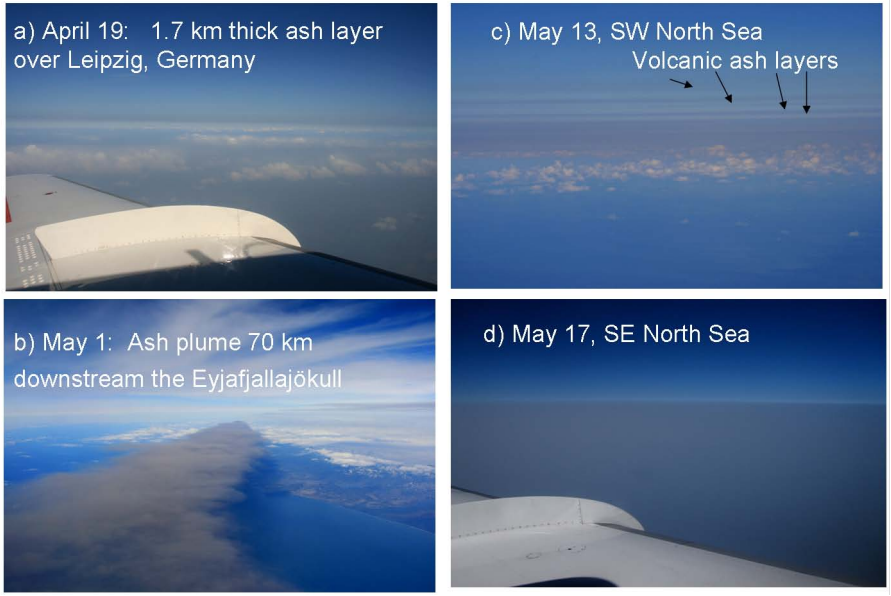

Fig. 11. Photos showing elevated volcanic ash layers (**a** and **c**), the fresh VA plume **(b)** and a deep VA layer **(d)** at various times and positions, and with various viewing directions as indicated. **(a)** 15:07 UTC 19 April 2010, 51.51° N, 12.44° E, 4.25 km, west; **(b)** 12:49 UTC 1 May, 63.18° N, 18.67° W, 6.7 km, northwest; **(c)** 14:09 UTC 13 May, 53.59° N, 1.04° E, 5.16 km, west; **(d)** 15:54 UTC 17 May, 52.70° N, 2.83° E, 6.39 km, southwest. The positions are identified in Fig. 3.

ACPD
10, 22131–22218, 2010

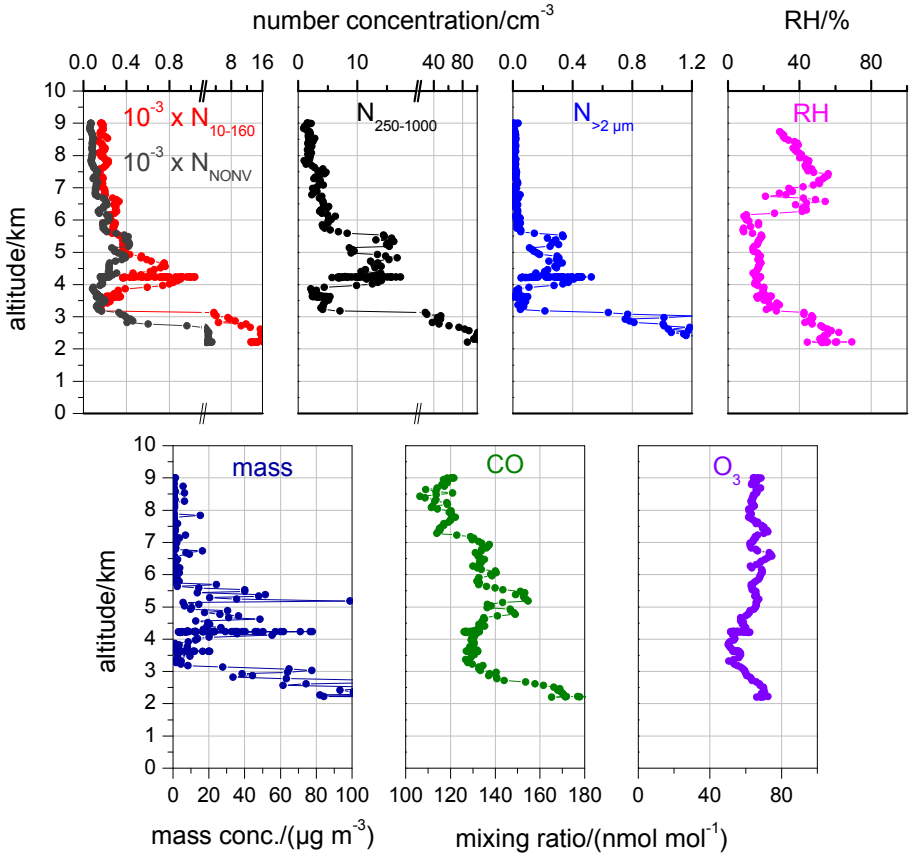

Fig. 12. Number concentrations of aerosols of various sizes, relative humidity, mass concentration (case N), and trace gases concentrations versus altitude over Leipzig, during Falcon descent, 14:51:00–15:28:00 UTC, 19 April 2010.

ACPD
10, 22131–22218, 2010

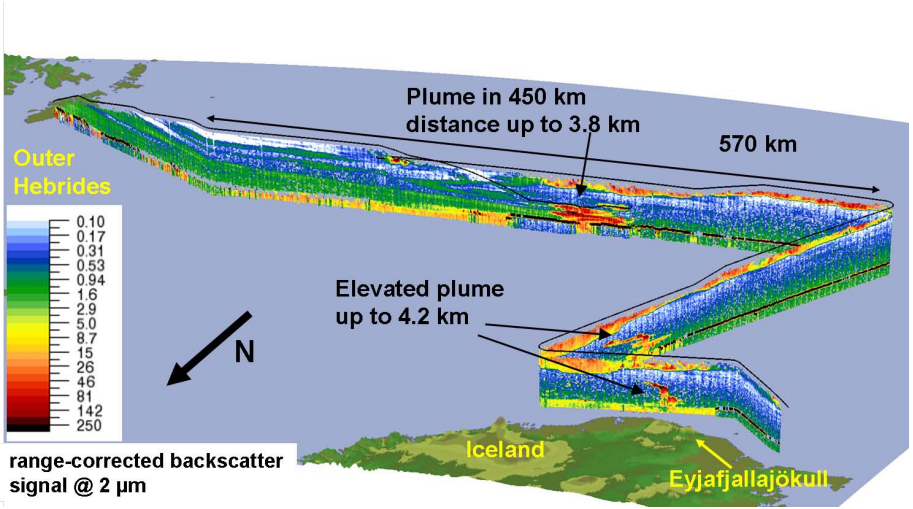

Fig. 13. Volcano plume cross-sections in Lidar perspective plot of range corrected backscatter along flight path from Iceland to Scotland, 2 May 2010.

ACPD
10, 22131–22218, 2010

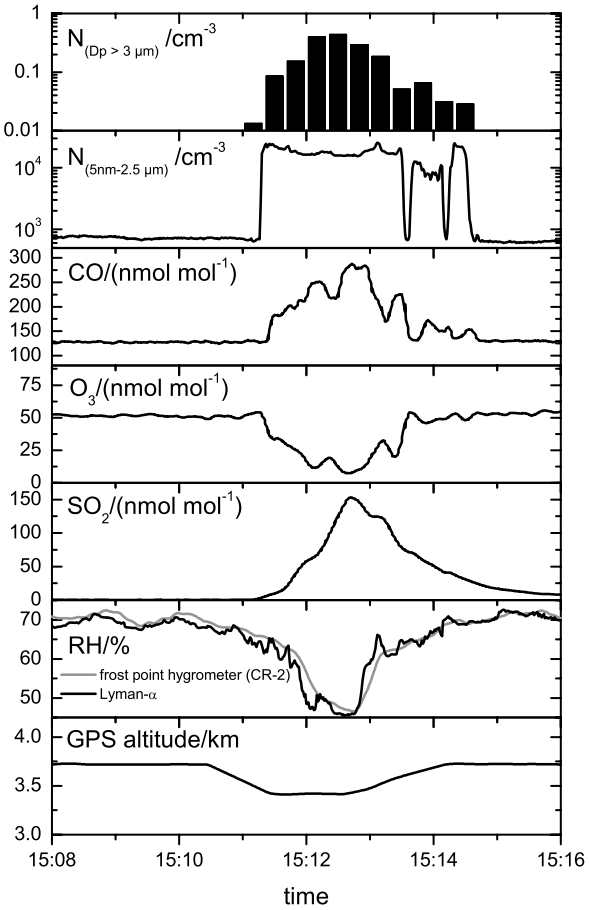

Fig. 14. Time series of aerosol number concentrations *N* in two size ranges, trace gas mixing ratios of CO, O_3, and SO_2, relative humidity RH from the two hygrometers, and flight altitude during the measurements over the North Atlantic versus UTC time on 2 May 2010.

ACPD
10, 22131–22218, 2010

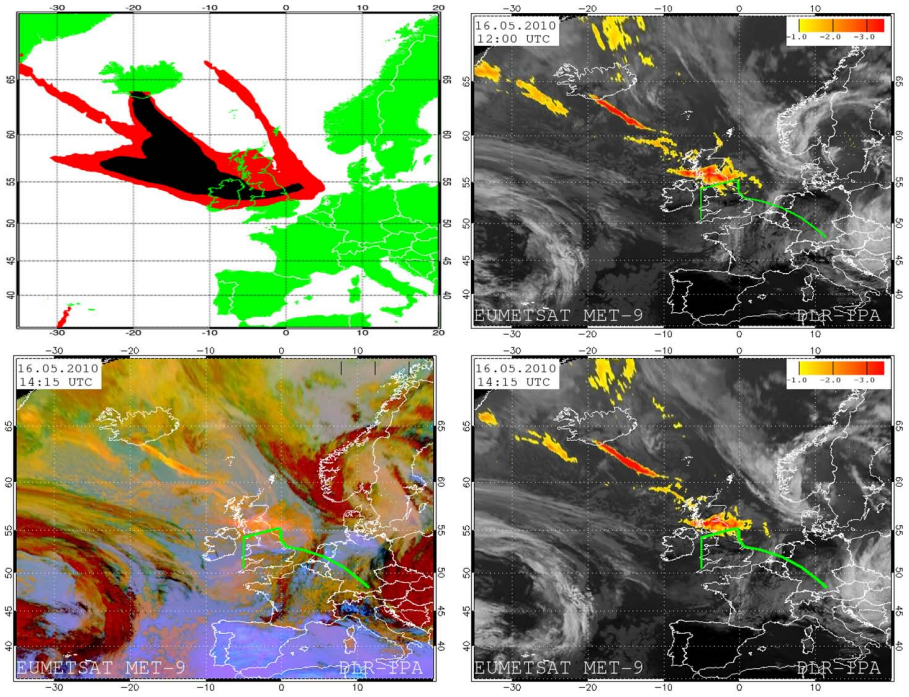

Fig. 15. Comparison of VAAC prediction for flight levels 0–6 km, issued 12:00 UTC 16 May 2010 (top left) together with various ash detection results based on Meteosat-8 SEVIRI data, in Mercator projection, including the Falcon flight path (green line). Top: 12:00 UTC 16 May 2010; bottom: 14:15 UTC 16 May 2010. Right panels: Ash product based on brightness temperature difference 10.8–12.0 µm in combination of smoothing and threshold −1.0 K. The grayscale background represents the 10.8 µm brightness temperature. Bottom left: Dust composite, as described in text. Ash appears orange in this composite.

ACPD
10, 22131–22218, 2010

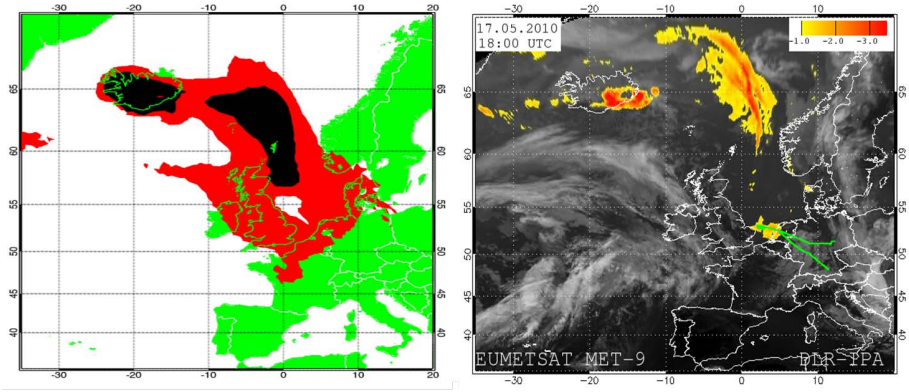

Fig. 16. VAAC prediction (issued at 18:00 UTC 17 May 2010) and Meteosat VA analysis including the Falcon flight path for 18:00 UTC 17 May 2010.

ACPD
10, 22131–22218, 2010

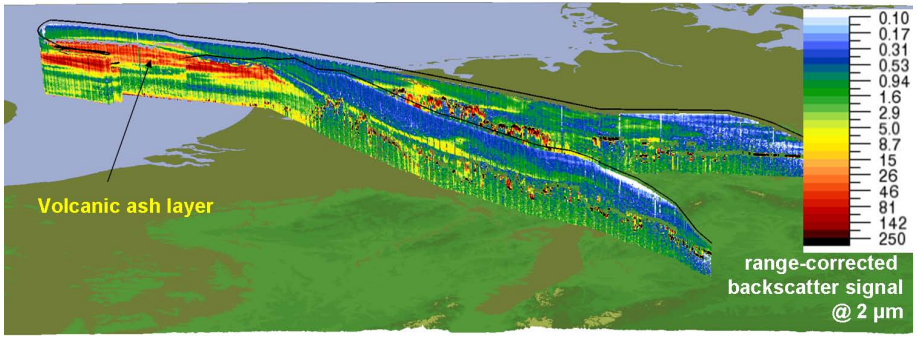

Fig. 17. Volcanic ash layers (red colors) cross-sections in Lidar perspective plot of range corrected backscatter along flight path from Leipzig (Germany) to the North Sea and back to Oberpfaffenhofen near Munich (Germany), 17 May 2010, afternoon. The flight altitude above the North Sea was 8.4 km.

ACPD
10, 22131–22218, 2010

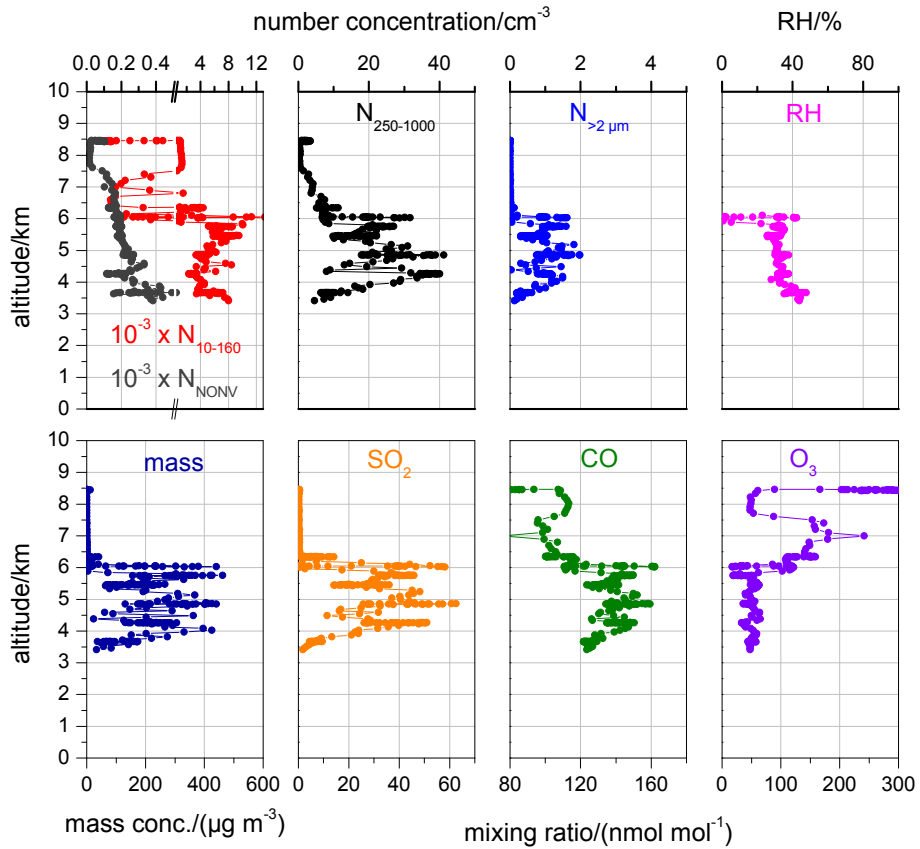

Fig. 18. Number concentrations of aerosols of various sizes, relative humidity, ash particle mass concentration (case N), and mixing ratios of sulfur dioxide, carbon monoxide and ozone versus altitude during Falcon descent over the North Sea, 15:41:00–16:32:00 UTC 17 May.

ACPD
10, 22131–22218, 2010

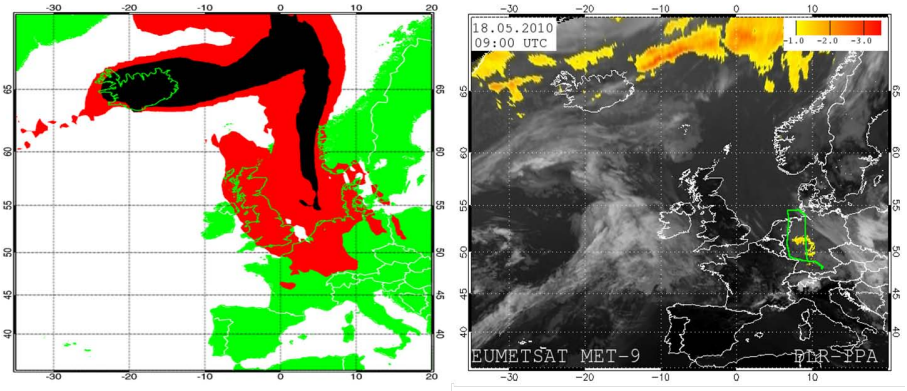

Fig. 19. VAAC prediction (issued at 06:00 UTC 18 May 2010) and Meteosat VA analysis for 09:00 UTC 18 May 2010, including the Falcon flight path.

ACPD
10, 22131–22218, 2010

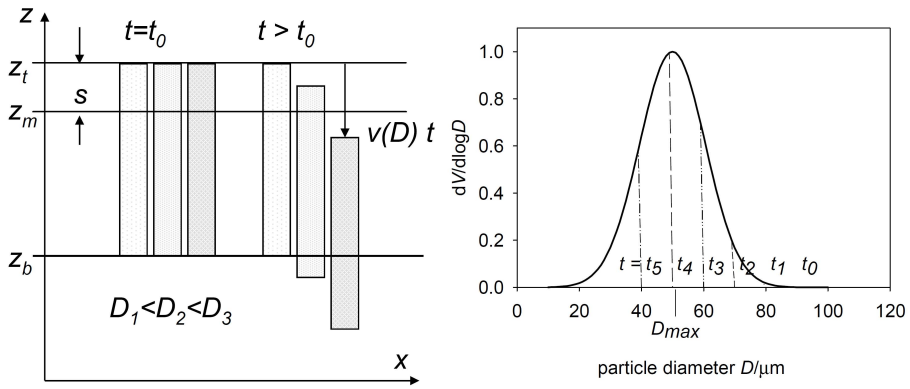

Fig. 20. Schematic explaining the formation of volume-size spectra with sudden cut-off near the largest measured diameter D. The left panel shows a horizontal ash layer at two times, t_0 and $t>t_0$. The levels of plume top (z_t), plume bottom (z_b), and level of measurement (z_m), are identified, with vertical separation $s=z_t-z_m$. The three rectangles show plume segments with different particle sizes – separated in x-direction for illustration. For $t>t_0$ the segment with largest particles has been sedimented uniformly over the largest distance $v(D)t$. The right panel shows the volume-size distribution starting from an arbitrary initial distribution with maximum diameter D_{max} at $t=t_0$. Because of sedimentation, a cut-off forms and gradually ($t=t_1$, t_2, etc.) moves to smaller diameters, so that after some time a volume distribution with maximum at this cut-off evolves.

ACPD
10, 22131–22218, 2010

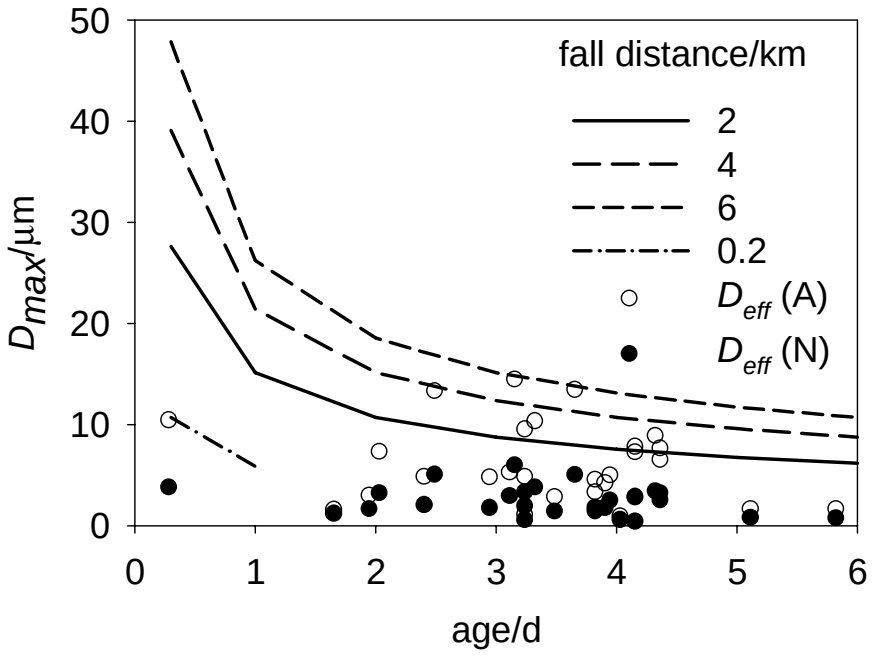

Fig. 21. Sedimentation-limited particle diameter D_{max} as a function of plume age and fall distance below plume top height. Also plotted are the effective diameters D_{eff} diagnosed from the FSSP data for absorbing (A) and non-absorbing particles (N).

ACPD
10, 22131–22218, 2010

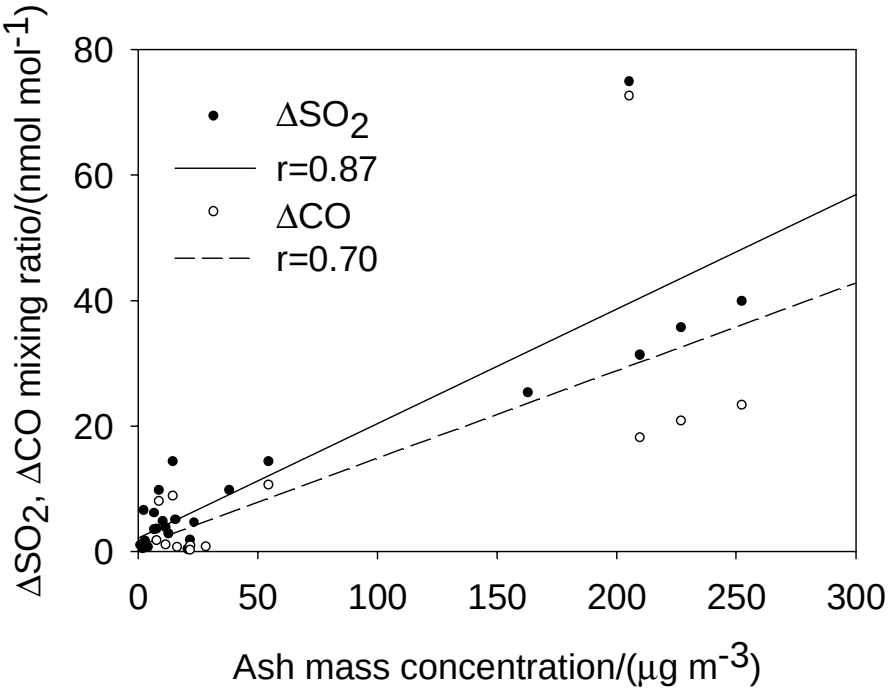

Fig. 22. Correlation between SO_2 and CO mixing ratio increases over background with ash mass concentration (analysis for non-absorbing particles). The points in the upper part of the diagram with largest gas mixing ratios result from the measurements of 2 May, with smallest plume age (7–12 h). The legend identifies the correlation coefficients *r* of the linear fits.

ACPD
10, 22131–22218, 2010

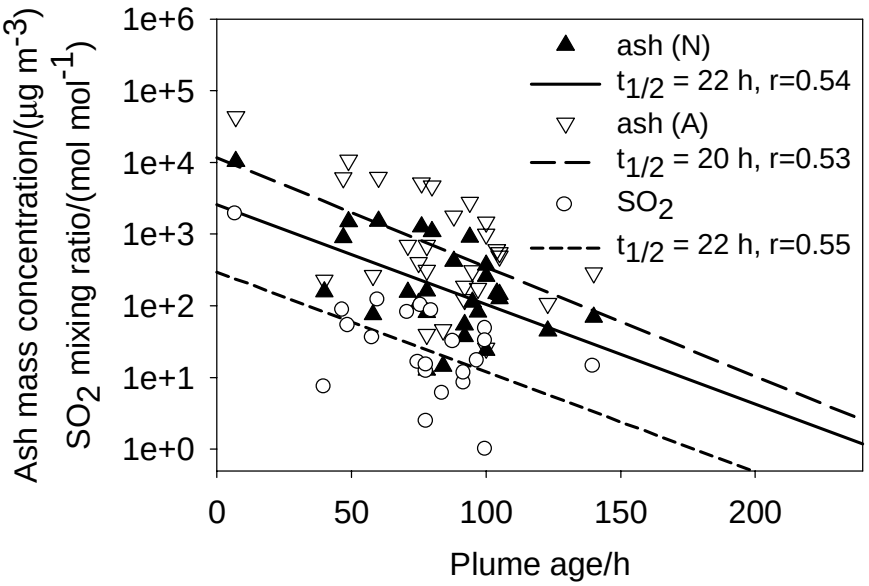

Fig. 23. Ash mass concentration and SO_2 mixing ratio versus plume age. The legend identifies the half value times $t_{1/2}$ and the correlation coefficient of the linear fits.

ACPD
10, 22131–22218, 2010

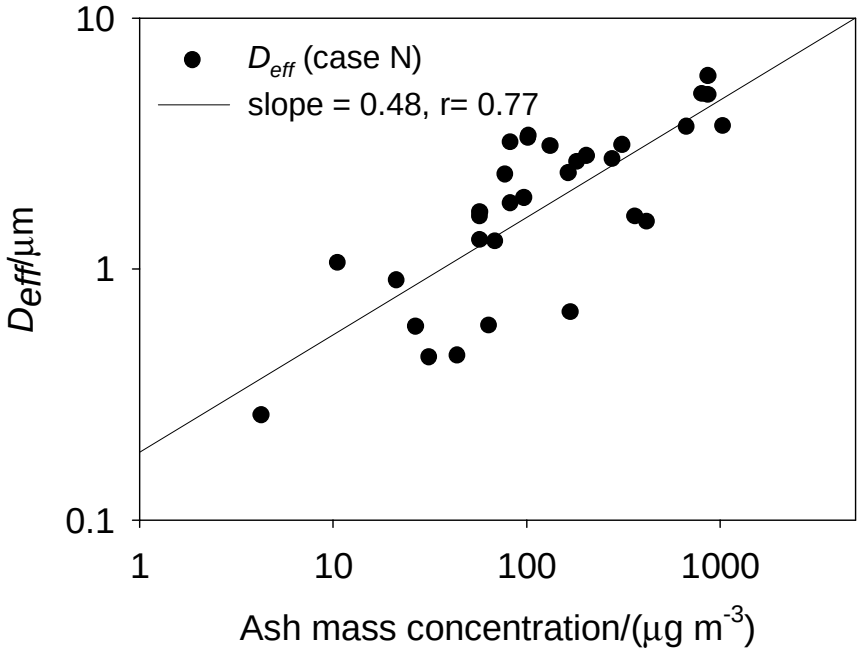

Fig. 24. Effective diameter D_{eff} versus ash mass concentration (based on accumulation and coarse mode particles; FSSP data analyzed for non-absorbing particles). The slope and correlation coefficient r of a linear interpolation is given.

ACPD
10, 22131–22218, 2010